Title

Along-the-channel modeling and analysis of PEFCs at low stoichiometry: Development of a 1+2D model

Authors

Pant, LM
Gerhardt, MR
Macauley, N
et al.

Publication Date

2019-12-05

DOI

10.1016/j.electacta.2019.134963

Peer reviewed

Along-the-Channel Modeling and Analysis of PEFCs at Low Stoichiometry: Development of a 1+2D Model

Lalit M. Pant[a], Michael R. Gerhardt[a], Natalia Macauley[b], Rangachary Mukundan[b], Rodney L. Borup[b], Adam Z. Weber [a,*]

[a] *Energy Conversion Group, Energy Technologies Area, Lawrence Berkeley National Laboratory, Berkeley, CA 94720, USA*

[b] *Los Alamos National Laboratory, Los Alamos, NM 87545, USA*

Water management remains a key challenge in polymer-electrolyte fuel cells (PEFCs). In this work, a pseudo 3-D (1+2D) model is developed to account better for changes of water management along the channel, as well as verify the possibilities of using differential cells for data capture. An accurate 2-D membrane-electrode-assembly (MEA) model is developed for differential cell modeling, which is combined with an along-the-channel stepping algorithm to account for down the channel changes in pressure, temperature, reactant concentration, and relative humidity. Variations in cell performance along the channel due to changes in operating conditions are characterized quantitatively and optimized. The 1+2D model is found to be critical at dry and low stoichiometry cell operations, where along the channel

** Corresponding author: AZWeber@lbl.gov (Adam Z. Weber)
Phone: +1 (510) 486-6308

hydration was found to increase cell performance for dry inlet conditions, which is also highly coupled to transport through the membrane. Overall, the study identifies gaps between differential and integral cells and highlights the need for better models to understand integral cell performance and water management.

1. Introduction

Polymer-electrolyte fuel cells (PEFCs) have gained significant interest as an energy-conversion technology [1]; however, further improvements in performance and durability are required for commercialization [2]. Diagnostic methods are critical to analyze cell performance and identify underlying mechanisms that control the performance and durability. Cell diagnostic methods consist of experimentally probing cell behavior, which then can be deconvoluted using a mathematical model. Cell polarization curves are an exemplary metric and diagnostic used for this purpose [3]. However, full cells suffer from changes in composition, temperature, etc. in the flow direction, thus making comparisons of different components and reproducibility problematic. Due to these issues, there is active research in the development of differential or zero-gradient cells for component diagnostics and characterization. Differential conditions require high stoichiometry and smaller cell sizes to ensure minimal changes in flow conditions along the channel [4]. It is the hope that one can develop a transfer function to bridge the gap between differential cell experiments and larger integral cell performance, where along-the-channel variations occur,

such that one only needs such differential-cell data. To understand accurately the underlying phenomena from the experimental data, physics-based mathematical modeling can be used, as long as they consider the relevant physics and any changes down the channel. Furthermore, such models can be used to ascertain when differential cell conditions exist, an objective of this paper.

Numerous modeling approaches have been presented in literature to simulate PEFC operation. The earliest modeling approaches used analytical models [5-8]. While these models have been useful to explain model system behavior at limiting cases [9-13], they have primarily focused on only a few of the phenomena. Furthermore, in order to be able to solve the system of equations, several simplifying assumptions are made, due to which these models cannot account for complex interactions between different underlying mechanisms. Numerical modeling techniques such as finite difference methods (FDM) and finite element method (FEM) provide a way to solve complex systems of partial differential equations. This allows the use of detailed mathematical models for all underlying phenomena. The initial numerical modeling approaches for PEFCs employed a 1-D modeling scheme for simplicity and reduced computational time [14-22]. Initial models assumed single-phase isothermal conditions and simple membrane transport model, where membrane was assumed to be fully hydrated [14, 16]. To improve upon these models, Weber and Newman [17], [18, 19] presented a membrane transport model to accurately account for water and proton

transport in ionomer. They also presented two-phase and non-isothermal transport models to account for presence of liquid water in the porous media using pore-size distribution models [20-22]. While these models provide some insight into the effects of each mechanism on performance, they do not account for down the channel changes and rib/channel effects. 1-D models of the catalyst coated membrane (CCM) have been combined with 3-D models of gas-diffusion layer (GDL) to account for some of these factors [23]; however, these methods are time consuming and not as accurate as higher dimension models.

Several two-dimensional macro-homogeneous models of membrane electrode assembly (MEA) have been proposed in literature that account for the physics in all porous layers and membrane, and also account for the effect of rib/channel asymmetry. Natarajan and Nguyen [24] presented a 2-D model of the cathode. The model accounted for rib/channel effects and assumed the catalyst layer as a simple interface without accounting for transport. Sun, Peppley and Karan [25] developed a full 2-D cathode model accounting for CL microstructure using an agglomerate model. Over time, further improvements over these models have been reported. These include: inclusion of anode [26], nonisothermal model [27-29], two-phase transport [30], and multiscale catalyst layers [31-35]. These current models have been used for studying the effect of several operating and structural parameters on PEFC performance [31-35]. These models accurately account for all macroscale physics and rib/channel effects, and are well suited for

diagnostics of differential cells; however, they do not account for along-the-channel variations in integral cells.

To account for down the channel variations, 2-D models have been presented in literature with one of the directions along the flow channels and another across the MEA assembly [22, 36-42]. While these models can take into account along-the-channel variations, the rib/channel effects are not considered. Futter, Gazdzicki, Friedrich, Latz and Jahnke [43] presented a 2-D along-the-channel model with accurate kinetics and membrane transport model, which was used to explain impedance spectroscopy data; however, most of these 2-D models use simplistic reaction kinetics and membrane transport models [36-41] and are not on par with current 2-D MEA cross-section models discussed above.

Several 3-D cell models have been proposed in literature to overcome the limitations of both types of 2-D models discussed above. The 3-D models can account for along-the-channel variations in properties, as well as the flow-field geometry. One of the first 3-D models was presented by Dutta, Shimpalee and Zee [44] to understand the effect of GDLs on cell current. 3-D models are best suited to analyze the effect of flow field geometry on cell performance. Um and Wang [45] showed that for parallel flow fields, the interaction between channels are insignificant, while they are critical for cell performance in interdigitated flow fields. Several other 3-D models have been reported to study channel configuration [46, 47], GDL effects [48],

water management [49-52], heat management [52], and agglomerate microstructure [53]. All of these models however focus their computational complexity in flow fields and use very simple MEA physics. Furthermore, due to their computational cost, only a small section of the cell can be simulated, making them impractical for full-cell simulations.

Along-the-channel marching methods combined with MEA cross-section models have been extensively used to model complete cells [42, 54-61]. These methods use 1-D or 2-D MEA cross-section models at each channel segment, and use mass, momentum, and energy balance equations to compute conditions down the channel. These methods provide higher accuracy than conventional MEA cross section models while being much less expensive than full 3-D models. Most of these type of models reported in literature use a simple 1-D MEA model [42, 54-59], which are used to understand the effect of down-the-channel variations on cell performance, water management, and crossover through membrane. Natarajan and Van Nguyen [60] presented an along-the-channel marching model with a 2-D cathode model. The model shows the effect of flooding in cells and importance of along the channel modeling. To our knowledge, no along-the-channel models have been reported in literature with complete 2-D MEA models.

This article is aimed at developing a pseudo 3-D (1+2D) along-the-channel PEFC model. The 1+2D model builds on top of previously reported 2-D MEA

model by our group [31, 62]. This article also aims to validate the model against experimental data, and use the validated model to compare differential and integral diagnosis methods and their applicability in general, including identification of the onset of differential conditions. The rest of the article is organized as follows: section 2 describes the 2-D MEA model in detail followed by the details of 1+2D model in section 3 A brief overview of the experimental method and conditions is given in section 4Next, section 5 presents the results. The validation studies are presented followed by different parametric studies using the 1+2D model. Finally, a summary of the article is provided.

2. 2-D Mathematical Model of MEA Cross Section

2.1. Assumptions

The 2-D continuum model used in work is based on previous work by Balliet and Newman [27] and Zenyuk, Das and Weber [31]. The model is subject to the following assumptions:

1) Steady-state operation
2) Macrohomogeneous modeling approach is valid assuming that all domains contain representative elementary volumes (REVs)
3) Ideal gas assumption is valid for gas phase species and total mixture
4) Liquid flow is assumed to be capillary driven, incompressible Newtonian flow
5) Water phase change in pores is driven by gradient in chemical potential of liquid and vapor

6) An interfacial resistance is assumed at ionomer-pore interface, which controls water adsorption/desorption
7) Oxygen reduction reaction (ORR) is governed by Tafel kinetics
8) A spherical agglomerate based approach is used to estimate ORR kinetics with mass transfer
9) Butler-Volmer (BV) kinetics accurately describes hydrogen reduction reaction (HOR)
10) Conduction is the prominent heat transfer mechanism in MEAs, all contacting phases are at the same temperature at each point, and convective heat transfer is negligible [28].

2.2. Governing equations

A two-phase, nonisothermal model of the MEA cross section is used, where the MEA cross-section domain is shown in Fig. 1. Symmetry is used in *y*-direction, and therefore only half of the land and channel segment is included in the modeling domain. The governing transport equations are given as:

$$\nabla\cdot\left[-\rho_G\omega_i\sum_k\widetilde{D}_{ik}\left(\nabla x_k+\frac{1}{p_G}\left(x_k-\omega_k\right)\nabla p_G\right)\right]+\rho_G u_G\cdot\nabla\omega_i=R_i,\forall i,k\in[H_2 \quad (1)$$

$$\nabla\cdot\left[-\rho_G\frac{k_{r,G}k_0}{\mu_G}\nabla p_G\right]=R_G, \quad (2)$$

$$\nabla\cdot\left[-\rho_L\frac{k_{r,L}k_0}{\mu_L}\nabla p_L\right]=R_L, \quad (3)$$

$$\nabla\cdot\left[-\sigma_s^{eff}\nabla\phi_s\right]=j_{rxn,s}, \quad (4)$$

$$\nabla\cdot\left[\left(1-S_m\right)\left(-\kappa_{m,V}^{eff}\nabla\phi_m-\frac{\kappa_{m,V}^{eff}\xi_{m,V}^{eff}}{F}\nabla\dot{\mu}_w\right)+S_m\left(-\kappa_{m,L}^{eff}\nabla\phi_m-\frac{\kappa_{m,L}^{eff}\xi_{m,L}^{eff}}{F}\nabla\right.\right. \quad (5)$$

$$\nabla\cdot\left[\left(1-S_m\right)\left(\frac{-\kappa_{m,V}^{eff}\xi_{m,V}^{eff}}{F}\nabla\phi_m-\left(\alpha_{m,V}^{eff}+\frac{\kappa_{m,V}^{eff}\left(\xi_{m,V}^{eff}\right)^2}{F^2}\right)\nabla\dot{\mu}_w\right)+S_m\left(\frac{-\kappa_{m,L}^{eff}\xi_{m}^{ei}\right.\right. \quad (6)$$

$$\nabla\cdot\left[-k_T^{eff}\nabla T\right]=Q_{gen}. \quad (7)$$

with the various symbols explained in the nomenclature section. Details of the properties used in transport modeling are discussed in following sections.

2.2.1. Molecular diffusion.

Molecular diffusion is modeled using species mass conservation, and Stefan-Maxwell equation [63] given by Eq. (1). The convective velocity u_g is obtained from gas mixture transport given by Eq. (2). The coefficient $\widetilde{D}_{ik}$ is mass fraction dependent inverted Stefan-Maxwell coefficient. For example, for a three component system, the inverted coefficient is defined as [31, 63]

$$\widetilde{D}_{12}=\frac{\frac{\omega_1(\omega_2+\omega_3)}{x_1D_{23}^{eff}}+\frac{\omega_2(\omega_1+\omega_3)}{x_2D_{13}^{eff}}-\frac{\omega_3^2}{x_3D_{12}^{eff}}}{\frac{x_1}{D_{12}^{eff}D_{13}^{eff}}+\frac{x_2}{D_{12}^{eff}D_{23}^{eff}}+\frac{x_3}{D_{13}^{eff}D_{23}^{eff}}}, \quad (8)$$

where each effective diffusion coefficient D_{ij}^{eff} can be given as

$$D_{ij}^{eff}=\frac{\epsilon_G}{\tau_G}D_{ij}, \quad (9)$$

$$\epsilon_G=\left(1-S_L\right)\epsilon_v, \quad (10)$$

$$\tau_G=\epsilon_G^{-\beta_{\tau,G}}. \quad (11)$$

The gas occupied volume fraction, ϵ_G, accounts for the liquid saturation S_L. Saturation of each layer is obtained using saturation-capillary pressure relations, i.e., water-retention curves. The tortuosity exponents, $\beta_{\tau,G}$ for each layer is are given in Table 1. The bulk molecular diffusion coefficients, D_{ij} for different gas pairs are expressed in Table S1 (supplementary material).

2.2.2. Gas mixture transport

The mixture convection is modeled using mass conservation and Darcy's law given by Eq. (2). The common gas transport properties are given in supplementary material (section 2). The mixture density and viscosity calculations are based on ideal gas assumptions [64]. The relative permeability is given as

$$k_{r,G} = S_G^{\beta_G} \equiv \left(1 - S_L\right)^{\beta_G}, \tag{12}$$

where the saturation exponent β_G for each layer is given in Table 1.

2.2.3. Liquid-water transport

Liquid-water transport is also modeled using Darcy's law and mass conservation, given by Eq. (3). The liquid properties used are given in supplementary material (section 3). The relative liquid permeability is given as

$$k_{r,L} = S_L^{\beta_L}, \tag{13}$$

where the relative permeability exponent β_L for each layer is given in Table 1.

2.2.4. Electron transport

Electron transport is modeled using Ohm's law and charge conservation, given in Eq. (4). Effective electronic conductivity is estimated as

$$\sigma_s^{eff} = \frac{\epsilon_s}{\tau_s}\sigma_s, \tag{14}$$

$$\tau_s = \epsilon_s^{-\beta_{\tau,s}} = \left(1 - \epsilon_v\right)^{-\beta_{\tau,s}}. \tag{15}$$

The bulk conductivity σ_s and tortuosity exponent $\beta_{\tau,s}$ are discussed in Table 1.

2.2.5. Water and proton transport in ionomer/ electrolyte-membrane

The electrolyte membrane is made of the proton conducting ionomer. The ionomer is also present in the catalyst layers. Water and proton transport in the ionomer (both: CL and membrane) is modeled using concentrated solution theory [18], mass conservation, and charge conservation equations. Equations (5) and (6) show the proton and water transport in ionomer respectively. It is assumed that transport occurs in parallel between vapor equilibrate and liquid equilibrated parts of the ionomer. Bulk conductivity and water uptake vary for different ionomers, and therefore are estimated by fitting the experimental data to the model if not available. Other properties and relations used in transport modeling are given in Table S2 (supplementary material).

2.2.6. Energy transport

The energy transport is modeled using heat conduction and energy conservation given by Eq. (7). Since convective heat transport is negligible, it has been omitted [28]. For bipolar plates and porous layers, experimentally measured effective thermal conductivities of different layers are used in the formulation. The net thermal conductivity for the ionomer is obtained assuming parallel heat transport through liquid water and bulk ionomer.

$$k_{T,m}^{eff} = \epsilon_w^{1.5} k_{T,L} + \left(1-\epsilon_w\right)^{1.5} k_{T,m}, \qquad (16)$$

where $k_{T,L}$ is thermal conductivity of liquid water (supplementary material, section 3), and $k_{T,m}$ is thermal conductivity of bulk membrane given in Table 1.

2.2.7. Transport properties of the cell components

Transport properties described in the previous sections depend on bulk properties and various correlation exponents. The various transport properties and exponents are listed in Table 1. Properties such as volume fractions also depend on liquid saturation in each porous layer, which is calculated using capillary pressure,

$$p_C = p_L - p_G. \tag{17}$$

Water-retention curves for each porous layer are given in supplementary material (section 5, Fig. S1). Liquid saturation for any capillary pressure can be obtained and used to estimate gas- and liquid-phase properties.

2.3. Source Terms

A summary of the source terms for the governing equations (Eqns. (1)-(7)) is given in Table 2. A detailed explanation of the different source terms is given in following subsections.

2.3.1. Water evaporation/condensation

Water phase change is modeled using chemical-potential equilibrium between liquid and gas phase. The rate of evaporation is given as

$$R_v = \begin{cases} k_{ev}\left(\acute{\mu}_L - \acute{\mu}_V\right) if\ \acute{\mu}_V > \acute{\mu}_L (condensation), \\ k_{ev}\left(S_L - S_{L,res}\right)\left(\acute{\mu}_L - \acute{\mu}_V\right) otherwise (evaporation). \end{cases} \quad (18)$$

The chemical potentials, $\acute{\mu}_L, \acute{\mu}_V$ are given in supplementary material (section 6). The evaporation/condensation constant k_{ev} is given in Table 3. It is chosen high enough to ensure quick equilibrium between liquid and vapor while keeping the numerical method stable. This high value of k_{ev} is also consistent with large liquid-vapor interface area at most saturations [35, 65]. The residual saturation term ($S_{L,res}$) in evaporating conditions is used to ensure that liquid water is present (higher than residual saturation) to evaporate.

2.3.2. Membrane water absorption/desorption

The water desorption/absorption from membrane to pore phase is modeled in a similar way to that of evaporation. Equilibrium between chemical potential of water in membrane and pore is assumed. We also assume that membrane water is in equilibrium with both liquid and vapor in pores, i.e., parallel desorption pathways. The desorption rates are then given as

$$R_{V,m} = k_{V,m}\left(\acute{\mu}_w - \acute{\mu}_V\right), \quad (19)$$

$$R_{L,m} = \begin{cases} k_{L,m}\left(\acute{\mu}_w - \acute{\mu}_L\right) if\ \acute{\mu}_V > \acute{\mu}_L, \\ 0\, otherwise. \end{cases} \quad (20)$$

The liquid desorption pathway is open only when saturation conditions exist, i.e. $\acute{\mu}_V > \acute{\mu}_L$. The absorption/desorption coefficients are given in Table 3.

2.3.3. Anode Reaction Kinetics

The hydrogen oxidation reaction (HOR) is modeled using Butler-Volmer equation. The volumetric anode current generation is given as [31, 66],

$$j_a=(1-S_L)A_{v,a}i_{0,a}\left[\frac{p_{H_2}}{p_{ref}}\exp\left(\frac{\alpha_{a,HOR}F}{RT}\eta_a\right)-\exp\left(\frac{-\alpha_{c,HOR}F}{RT}\eta_a\right)\right], \quad (21)$$

$$\eta_a=\phi_s-\phi_m. \quad (22)$$

where $A_{v,a}$ is the catalyst area per unit volume in anode. Other coefficients/properties are given in Table 3.

2.3.4. Cathode Reaction Kinetics

The oxygen reduction reaction (ORR) is modeled using Tafel kinetics combined with an agglomerate model. An illustration of the agglomerate structure in given in Fig. 1. A spherical ionomer filled core with Pt/C particles is assumed, which is covered by a uniform ionomer film. The volumetric agglomerate current density in agglomerate is given as [67]

$$j_{agg}=4F\acute{V}_{agg}\frac{p_{O_2}}{H_{O_2,m}}\left[\frac{1}{E_r k_c}+\frac{\delta_{agg}r_{agg}^2}{3D_{O_2,m}\left(r_{agg}+\delta_{agg}\right)}\right]^{-1}, \quad (23)$$

where the kinetic properties are given in Table 3. The expressions to obtain different agglomerate parameters are given in supplementary material (section 7). The reaction rate constant k_c is obtained using the Tafel kinetics as [67],

$$k_c=\frac{A_{v,c}i_{0,c}}{4F\left(1-\epsilon_v\right)\acute{V}_{agg}c_{O_2}^{ref}}\exp\left[\frac{-\alpha_{c,ORR}F}{RT}\eta_c\right], \quad (24)$$

where $A_{v,c}$ is catalyst area per unit volume in cathode, The cathodic overpotential is computed as,

$$\eta_c = \phi_s - \phi_m - E_{OCV}. \quad (25)$$

Once the volumetric agglomerate current is obtained, the current per unit volume of cathode catalyst layer can be obtained as,

$$j_c = j_{agg}\left(1 - S_L\right)\left(1 - \epsilon_v\right). \quad (26)$$

2.3.5. Heat Sources

Several sources of heat exist in different layers of the cell. The ohmic (Joule heating) due to electron/proton current is given as

$$Q_{ohm,s} = \frac{i_s \cdot i_s}{\sigma_s^{eff}}. \quad (27)$$

The Joule heating due to protonic current is given as

$$Q_{ohm,m} = \frac{i_m \cdot i_m}{\kappa_m^{eff}}. \quad (28)$$

The current and effective conductivity for solid/electrolyte phase are discussed in supplementary material (section 8). The heat of condensation is given by

$$Q_{ev} = -R_{ev} H_v, \quad (29)$$

where H_v is latent heat of water evaporation. For the membrane water, the adsorbed water is assumed to be in the liquid phase. Therefore, while the heat associated with liquid desorption is zero, consistent with water being in a condensed phase in the membrane, the heat associated with vapor desorption is assumed to be the same as evaporation, i.e.,

$$Q_{w,m} = -R_{v,m} H_v. \quad (30)$$

The heat of reaction for anode and cathode are given as

$$Q_{rxn,a} = j_a\left(\eta_a - \Pi_a\right), \quad (31)$$

$$Q_{rxn,c} = -j_c\left(\eta_c + \Pi_c\right), \quad (32)$$

Where the Peltier coefficients (Π) are given in Table 3 .

2.4. Boundary Conditions

Table 4 shows the boundary conditions for different variables at various boundaries. The boundary condition for liquid water uses a hyperbolic step function, which ensures than the liquid flux at the interface is zero until p_L is above the breakthrough pressure. The value of k_L is selected high enough to ensure that when breakthrough pressure is reached, the value of liquid pressure matches the breakthrough pressure (i.e., Dirichlet type B.C.).

3. Integral Modeling of a Single Cell

3.1. Overview

To simulate the cell at integral conditions, the entire cell needs to be simulated, as the conditions change along the channel. Since a complete 3-D simulation is computationally expensive, a segmented approach is used. Fig. 2 shows an illustration of the segmented cell approach for a co-flow serpentine channel cell. The segmented approach models the integral cells as interconnected segments, where each segment is small enough to be assumed as a differential cell. The 1+2D model uses the 2-D MEA model described in previous section combined with an along-the-channel stepping method as shown in Fig. 2(d-e). The approach takes into account the following assumptions**:**

- Co-flow parallel/serpentine channels; different flow configurations will be part of future studies [42].
- No in-plane transport in z-direction outside of the channel; only the properties at the channel boundary get updated at each step, which is consistent with significant length scale differences.
- Each segment has uniform conditions in the channel, i.e., well mixed.

At each step along the channel (denoted as 1,2 … N in Fig. 2(d)) the 2-D MEA model is solved. Using the 2-D model solution, consumption and production rates of species can be obtained. A step of size Δz is taken along z-direction, and conservation equations are used to estimate channel conditions at next step.

3.2. Along-the-channel model

While the inlet conditions for the first segment are known from the cell operating conditions, the outlet of each segment needs to be computed using mass, momentum, and energy conservation equations. Fig. 3 shows a control-volume representation of the cell segment showing all of the fluxes and source/sink terms. Using the conservation equations, estimation of each operating condition at the segment outlet is discussed below.

3.2.1. Reactant species mass conservation

As shown in Fig. 3, mass conservation of reacting species R(hydrogen, oxygen) in a cell segment can be given as,

$$\dot{N}_{R,out} = \dot{N}_{R,\in¿ - R_{R,cons},¿} \tag{33}$$

where $R_{R,cons}$ is estimated by integrating reaction rate in given CL,

$$R_{R,cons} = \Delta z \int_{x=0}^{L_{CL}} \int_{y=0}^{d_h} R_R'' \, dx \, dy, \tag{34}$$

$$R'' = \begin{cases} \frac{j_a}{2F} Anode, \\ \frac{j_c}{4F} Cathode. \end{cases} \tag{35}$$

L_{CL} is catalyst layer thickness and d_h is height of the domain shown in Fig. 1.

3.2.2. Diluting species mass conservation

The diluting species N_2 is non-reacting and therefore the flux remains constant in each segment,

$$\dot{N}_{N_2,out} = \dot{N}_{N_2,\in¿.¿} \tag{36}$$

3.2.3. Water mass balance

The water balance in each segment is given as,

$$\dot{N}_{w,out} = \dot{N}_{w,\in¿ + R_{w,ch},¿} \tag{37}$$

where $R_{w,ch}$ is the rate of net water production in segment given as

$$R_{w,ch} = \Delta z \int_{x=0}^{L_{CL}} \int_{y=0}^{d_h} (R_{V,m} + R_{L,m}) \, dx \, dy. \tag{38}$$

The net water mole fraction at outlet is given as

$$x_w^{out} = \frac{\dot{N}_{w,out}}{\dot{N}_{R,out} + \dot{N}_{N_2,out} + \dot{N}_{w,out}}. \tag{39}$$

The outlet relative humidity is estimated as

$$RH_{out} = min\left[1, \frac{x_{w,out} p_{G,out}}{p_{V,out}^{sat}}\right], \tag{40}$$

where $p_{V,out}^{sat}$ is the vapor saturation pressure at outlet, and is implicitly dependent on outlet temperature and outlet water content. Details on

obtaining saturation pressure are provided in supplementary material (section 9). Using the outlet relative humidity, vapor and liquid water fluxes can be estimated as

$$\dot{N}_{V,out}=\frac{RH_{out}p_{V,out}^{sat}}{p_{G,out}}\left(\dot{N}_{R,out}+\dot{N}_{N_2,out}+\dot{N}_{w,out}\right), \quad (41)$$

$$\dot{N}_{L,out}=\dot{N}_{w,out}-\dot{N}_{V,out}. \quad (42)$$

The molar fraction of reactant and diluent in outlet gas mixture can be estimated as

$$x_{R,out}=\frac{\dot{N}_{R,out}}{\dot{N}_{R,out}+\dot{N}_{N_2,out}+\dot{N}_{V,out}}, \quad (43)$$

$$x_{N_2,out}=\frac{\dot{N}_{N_2,out}}{\dot{N}_{R,out}+\dot{N}_{N_2,out}+\dot{N}_{V,out}}. \quad (44)$$

The amount of liquid water condensing in a given segment can be obtained as

$$\dot{N}_{L,cond}=\dot{N}_{L,out}-\dot{N}_{L,\in\dot{\iota}.\dot{\iota}} \quad (45)$$

3.2.4. Pressure loss

Assuming laminar flow, the pressure loss in a flow channel can be calculated as [68]

$$\frac{dp_G}{dz}=\frac{f_{\Re}}{2D_h}\rho_G v_G^2. \quad (46)$$

where the hydraulic diameter D_h is

$$D_h=\frac{4A_{ch}}{P_{ch}}\equiv\frac{4w_{ch}h_{ch}}{2\left(w_{ch}+h_{ch}\right)} \quad (47)$$

where w_{ch} and h_{ch} are the channel width and height, respectively. The friction factor $f_{\Re}$ is usually given in the form of $f/\Re$, where

$$\Re=\frac{\rho_g v_g D_h}{\mu_g}. \quad (48)$$

Substituting Eq. (50) into Eq. (46), we get the following expression for pressure loss,

$$\frac{dp_G}{dz} = \frac{f \mu_g v_g}{2 D_h^2}. \quad (49)$$

The factor f for small rectangular channels is determined to be [69]

$$f_{\Re} = 24\left[1 - 1.3553\left(\frac{h_{ch}}{w_{ch}}\right) + 1.9467\left(\frac{h_{ch}}{w_{ch}}\right)^2 - 1.7012\left(\frac{h_{ch}}{w_{ch}}\right)^3 + 0.9564 \quad (50)$$

The gas velocity in channel at any point can be obtained as,

$$v_g = \frac{\dot{N}_g}{c_g} \equiv \frac{RT\left(\dot{N}_{R,out} + \dot{N}_{N_2,out} + \dot{N}_{V,out}\right)}{p_G}. \quad (51)$$

To get the total pressure loss across a segment, Eq. (46) can be integrated along the segment length as,

$$p_{G,\in ¿} - p_{G,out} = \int_0^{\Delta z} \frac{f \mu_g v_g}{2 D_h^2} dz. ¿ \quad (52)$$

For small segments, we can assume that properties and variables across the segment change in a linear fashion. Eq. (52) can be converted into a summation,

$$p_{G,\in ¿} - p_{G,out} = \Delta z \frac{f \mu_g^{avg} v_g^{avg}}{2 D_h^2}, ¿ \quad (53)$$

where the average properties are

$$v_G^{avg} = R\left(T_{¿} + T_{out}\right) ¿ ¿ \quad (54)$$

$$\mu_g^{avg} = ¿ ¿ ¿ \quad (55)$$

Additional pressure drop occurs at the bends, which is given as [68]

$$\Delta p_{bend} = K_{bend} \frac{\rho v_G^2}{2}, \quad (56)$$

where K_{bend} is usually reported in literature for highly turbulent flows. In this work, a lower value of $K_{bend} = 0.2$ is used [68], as the Reynolds number is lower in cell channels. Shorting of flow has also been reported at the

serpentine bends which results in flow bypassing the bend and moving under the land to next channel [70]. This usually occurs when the pressure drop is higher in the bends making flow under the land favorable. This results in additional reactant transport to the catalyst layer and enhanced performance. While this phenomenon could be incorporated in the model as perhaps reactant mole fraction or pressure gain, it has been neglected in this work.

3.2.5. Energy conservation in the segment

The energy conservation in each segment is given as

$$\dot{H}_{out} = \dot{H}_{¿} + q_{¿,ch}. \quad (57)$$

The enthalpy flow rate can be obtained by summing the enthalpies of all gaseous and liquid species as

$$\dot{H}_{¿} = \sum_i \dot{N}_i \acute{C}_{p,i} T_{¿}, \quad (58)$$

$$\dot{H}_{out} = \sum_i \dot{N}_i \acute{C}_{p,i} T_{out}. \quad (59)$$

The molar specific heat for each species are given in supplementary material (section 10). The heat flow into channel from the MEA can be obtained as,

$$q_{¿,ch} = \Delta z \int h_{chan}(T - T_{chan}) - R_{R,cons} \acute{C}_{p,R} T_{avg} + R_{w,ch} \acute{C}_{p,V} T_{avg} + \dot{N}_{L,co} \quad (60)$$

which is a combination of convective heat transfer to channel from GDL and BPP, convective enthalpy transport by species production/consumption, and heat of phase change. T_{avg} is the average segment temperature. The heat flow out of the bipolar plate to the coolant is given as

$$q_{out,cool} = \Delta z \int_{y=0}^{d_h} h\left(T - T_{cool}\right) dy. \quad (61)$$

Once the outlet enthalpy is calculated, outlet temperature can be obtained,

$$T_{out} = \frac{\dot{H}_{out}}{\sum_i \dot{N}_i \acute{C}_{p,i}\big|_{out}}. \quad (62)$$

The outlet temperature calculations depend on T_{out} itself, making it an implicit problem. A recursive convergence loop is therefore used that is executed until the guessed and computed outlet temperatures are the same. The coolant temperature for the next row of segmented is also updated as

$$T_{cool,next} = \frac{\dot{N}_{cool} \acute{C}_{p,cool} T_{cool} + q_{out,cool}}{\dot{N}_{cool} \acute{C}_{p,cool}}. \quad (63)$$

4. Experimental Details

For the differential cell analysis, a 5 cm^2 area (3.45 cm x 1.47 cm) is exposed in the straight section near the outlet of a 50 cm^2 14-channel serpentine cell. The channels have dimensions of 0.508 mm (land) x 0.508 mm (channel) x 0.508 mm (depth). Fixed flow rates of 0.7 and 1.2 $L \cdot min^{-1}$ for H_2 and air, respectively, are used. For integral cell analysis, a quad serpentine fuel cell with 50 cm^2 MEA area is used for integral cell analysis. The channels have dimensions of 0.787 mm (land) x 0.787 mm (channel) x 1.016 mm (depth). Different flow rate combinations were used for understanding the effect of reactant flow/stoichiometry. A SIGRACET SGL 29 BC is used for GDL/MPL on each electrode. A Dupont Nafion® HP membrane with 22 μm thickness is used. The anode CL contains Pt (loading 0.1 $mg \cdot c\, m^{-2}$) on Graphitic carbon and Dupont DE 2020 ionomer (I:C 0.75). The

cathode CL contains Pt (loading 0.1 $mg \cdot c\, m^{-2}$) on high surface area carbon and Dupont DE 2020 ionomer (I:C 0.75). The MEAs were conditioned with a 16h hold at 0.6 V, 80C and 100%RH, after which four recovery procedures were performed, to desorb and wash out any impurities from the catalyst layers [71]. The anode ECSA is 51 $m^2 \cdot$¿, and cathode ECSA varies with RH due to varying hydration of primary pores within the carbon particles.

5. Results and Discussions

5.1. Cell Parameter Estimation from Differential Cell Modeling

One of the aims of this article is to understand if the differential analysis can capture the cell behavior at integral condition. To accomplish that, several cell parameters are estimated from the differential experimental data using the 2-D model. The same parameters will be then used for 1+2D model to see whether the prediction match the integral cell data. Most of the physical properties used in the model have been discussed in the previous sections. Table 5 shows the physical properties, parameters and operating conditions used in the analysis. A few of the crucial parameters are unknown and will be estimated from fitting the experimental data to the 2-D model.

All of the data sets were fit together to obtain best fit at different operating conditions. To obtain the cathode ECSA at different RH, the kinetic region was fit to the experimental data using ECSA as fitting parameter. Fig. 4 shows the estimated cathode ECSA at different relative-humidity (RH)

values. A minor increase is observed in ECSA with RH at unsaturated conditions; however, a significant increase is observed for 100% RH. This is understandable as the interior pores of high surface carbon are fully flooded at 100% RH making them accessible to protons and thereby increasing the available Pt area significantly [72]. While the ECSA would change locally in the CL depending on local water content, this is currently still being investigated experimentally. Based only on the polarization curves, the ECSA has been assumed to be a function of channel RH in this study. The sharp change between 80% and 100% RH can also poses a challenge, as the trend between these points is not known and more data is required. However, the fit values are within those reported in the literature [72].

The liquid- and vapor-equilibrated bulk conductivity of ionomer affect the ohmic region most significantly. The conductivity of the vapor-equilibrated ionomer is impacted by the water content in the ionomer, which is fit to experimental data. Figure S2 (supplementary material) shows the fitted water-uptake curve and a comparison with literature Nafion® membrane values [73]. The water uptake was found to be higher than Nafion®112 at lower RH, and marginally lower at RH greater than 0.75. The liquid equilibrated bulk ionomer conductivity was also fitted to capture the behavior at higher liquid saturation. The best fit was obtained for the following conductivity expression

$$\kappa_{m,L}=75\left[S\cdot m^{-1}\right]0.39^{1.5}\exp\left[\frac{15000\left[J\cdot m^{-1}\right]}{R}\left(\frac{1}{310[K]}-\frac{1}{T}\right)\right] \quad (64)$$

The temperature dependence of this expressions was kept the same as the reported for Nafion®112 [31]. The liquid equilibrated conductivity is 1.5 times higher than Nafion® 112 [31], consistent with the improvements expected for HP membrane.

Finally, the transport-limited region at 100% RH was used to estimate agglomerate properties. The best fit was obtained at δ_{agg}=4 nm, which is within expected values [74]. Fig. 5 shows the fitted polarization-curves against experimental data at different operating conditions. It should be noted that the numerical polarization curves are not individually fit to experimental data but have been globally fit across different RH values. A good fit is observed between experimental data and model estimations at all measured RH and temperatures.

5.2. Integral Cell Modeling

Once the cell parameters are estimated using differential data and 2-D model, the same parameters are used for integral cell modeling using the 1+2D model described earlier.

5.2.1. Understanding the Implications of 1+2D Model against Experimental Data

Experimental data on the integral 50 cm^2 cell was obtained at 40% and 80% inlet RH. Three flow rates were used at each RH: anode/cathode- 0.2/0.4 $L \cdot min^{-1}$, 0.4/0.8 $L \cdot min^{-1}$, and 1.0/2.0 $L \cdot min^{-1}$. The model uses the same parameters as in differential model, except the channel geometry, which is different as discussed in section 4. Since the ECSA is only fitted at few channel RH values, a linear interpolation is used in between (shown in Fig. S3(a) supplementary material).

Fig. 6 shows the comparison of the 1+2D model estimations with the experimental data at different operating conditions. At 40% RH, the model exhibits good agreement with experimental data at lower flow rates as shown in Fig. 6(a); however, at higher flow rates the model shows significant deviation from the experimental results, which is perhaps counter intuitive since high flowrates should approach differential conditions. However, comparisons of the high flowrate and differential data also exhibit differences, thus, there are some systematic issues between the two cell setups as discussed in more detail below. At lower flow rates, most of the oxygen is consumed at higher currents, which is evident in the stoichiometry values shown. This results in transport-limited behavior of the cell, which is accurately predicted by the 1+2D model. The disagreement at higher flow rate may be due to higher pressure drop in the serpentine channels that can result in higher in-plane transport that is unaccounted for by the 1+2D

model. Higher flow rates can also cause cell dry-out, resulting in higher ohmic losses then the model predictions.

Fig. 6(b) shows the comparison of the model estimation with the experimental data at 80% inlet RH. Like the 40% RH case, lower flow rates show better agreement. Again, the cell exhibits limiting behavior at lower flow rates due to reactant depletion and flooding, which is captured well by the model. The disagreement at higher flow rates is present in both: 40% and 80% RH cases, suggesting that the discrepancy is not likely due to cell dry-out as it should not be the case at 80% RH. There are several possible reasons for the discrepancy. While the differential cell has straight channels, the integral cell has serpentine channels. Furthermore, the Reynolds number in differential cell cathode is approximately 200, while in integral cell it is around 600. Combined together, this may create a completely different flow profile, velocity, and conditions in integral channels that are inherently different than the differential cell experiments and highlights the importance of using a model to translate among the different setups. Also, the thermal management and compression of the two cell setups are not necessarily identical. A better channel model or new differential experiments may be needed to capture the cell behavior at higher flow rates.

By comparing Fig. 6(a) and Fig. 6(b), it is seen that the 1+2D model at 80% RH overpredicts and demonstrates worse performance than 40% RH in the kinetic (i.e., high potential) region. To identify the source of discrepancy,

the performance of the integral cell was compared to differential cell at 80% RH (supplementary material, Fig. S4), and it is seen that the performance for all cases is the same in the kinetic region. As the kinetic region is primarily dependent on ECSA, it can be inferred that the ECSA is similar for integral and differential cases, which makes sense as it should be dominated more by MEA than operating flowrates in that regime. Under integral conditions, along-the-channel water accumulation will increase the channel RH as shown in Figure S5 (supplementary material). Based on the linear interpolation of ECSA (shown in Fig. S3(a), supplementary material), the 1+2D model predicts a much higher ECSA than at 80% RH, contrary to what experimental data suggests. Based on this, we estimate that the major increase in ECSA happens very near 100% RH (above 95% RH) resulting in different ECSA transition as shown in Fig. S3(b) (supplementary material). This transition does not affect the kinetic region in 40% RH integral cases, as the channel RH does not increase significantly (Fig. S6, supplementary material), resulting in accurate kinetic estimations in Fig. 6(a). Using the newer ECSA transition profile, new polarization curves were obtained as shown in Fig. 7. The new ECSA profile results in better fit for 80% RH, suggesting that a detailed study on ECSA analysis of high surface carbon is required, especially near saturation conditions. No significant change is observed for 40% RH cases as the new trend only affects the transport limited region.

5.2.2. Understanding the Effect of Flow Rate on Cell Performance and Limitations of a Differential Model

As seen in the above validation studies, reactant depletion and hydration along the channel are strong functions of the reactant flow rate and are critical to cell performance. To understand the effect of flow rate, the 1+2D model was used to simulate cell performance at several reactant flow rates. It is also of interest to know at which conditions along the channel changes become insignificant and differential mode is achieved.

Using the 1+2D model, simulations were run at 80°C, 40% and 80% RH, and various flow rates. Fig. 8 shows the performance of the cell at different flow rates and the comparison with a differentia cell simulation at same operating conditions. At high potentials (kinetic region), the cell performance is similar at all flow rates and at differential conditions. As discussed earlier and shown in supplementary material Figures S5-S6, the RH and mole fraction do not change significantly in the kinetic region. Furthermore, the RH-dependent ECSA also remains the same, causing the similar performance prediction at different flow rates.

At lower potentials (ohmic and transport-limited regions), the effect of flow rates on cell performance is more evident. Comparing between Fig. 8(a) and (b), it can be observed that the differential model demonstrates more deviation from integral data at drier conditions. To analyze reactant

utilization/limitation along the channel, the cathode stoichiometry at lowest simulation potential (highest current) was calculated. Table 6 shows the stoichiometry at maximum current for both 40% and 80% RH, and varying flow rates. The stoichiometry for low flow rates is near 1, suggesting complete consumption of cathode reactants and transport limited behavior in cell, which is also seen in the polarization curves (see Fig. 8); it is also evident that to obtain differential conditions at 40% RH requires higher stoichiometry than at 80% RH.

To understand the effect of flow rates in more detail, the variation of channel conditions and cell performance along the cell was studied. Fig. 9 shows the variation of local cell performance, and channel conditions along the channel at 0.3 V and 40% RH. As shown in Fig. 9(a), the cell performance initially increases along the channel, which is due to increasing channel RH shown in Fig. 9(b-c) and therefore better membrane hydration. Afterwards, the reactant depletion as shown in Fig. 9(d) results in a performance decrease. At low flow rates, the end of the cell is actual not participating significantly due to the low stoichiometry, which is actually determined using the average current. Thus, cell starvation conditions can exist near the flow outlet although the stoichiometry is somewhat above 1. Due to significant RH increase, the peak performance is much higher than performance at inlet segment which corresponds to a differential condition. At lower flow rates ($\dot{V}$ <1 $L \cdot min^{-1}$), along-the-channel variations are significant in terms of both:

mole fraction and relative humidity. At medium flow rates ($1<\dot{V}<4\ L\cdot min^{-1}$), the RH change along the channel is still significant while mole fraction changes less. Only at very high flow rates ($\dot{V}>4\ L\cdot min^{-1}$) none of the operating conditions change significantly along the channel.

Fig. 10(a-d) show the variation of local cell performance, and channel conditions along the channel at 0.3V and 80% RH. A minor increase in performance is observed in Fig. 10(a) before the cell becomes saturated and flooded (Fig. 10(b-c)). Afterwards, the performance continuously decreases due to reactant depletion as shown in Fig. 10(d). Since the inlet RH is already significantly high, net RH change along channel is not significant at any flow rate. Due to this, the 80% RH cases show better match against differential data. Comparing the 40% and 80% RH cases, it can also be seen that the best performance at low RH is obtained at medium flow rates: where the flow rates are low enough to allow RH increase along the channel while keeping the reactant depletion to a non-detrimental value. For higher RH however, higher flow rates can be used to minimize reactant depletion, as the channel hydration is less of a concern, unless channel flooding and reactant blockage (currently not incorporated in the model) becomes important.

To further compare the differential and integral studies, 1+2D simulations were carried out at 80C, 100% inlet RH, and varying flow rates. In these conditions, RH along the channel remains constant; however,

reactant depletion still causes the mole fractions to change. The average mole fraction along the channel can be estimated using a log-mean average of inlet and outlet, which can then be used in a differential model. The log-mean mole fraction is defined as:

$$x_{avg} = \frac{x_{¿} - x_{out}}{\log(x_{¿}) - \log(x_{out})}. \quad (65)$$

Fig. 11 shows the comparison of the 1+2D model based integral performance and the average mole fraction based differential model performance. The average mole fraction based differential analysis can accurately capture the behavior of integral cell for the fully saturated conditions. Therefore, in situations where RH change is minimal, a differential model with average mole fraction can be used to estimate integral cell performance. Overall, the different studies suggest that a simple 2-D model is usually not able to simulate accurately the integral cell, especially in low RH and low stoichiometry conditions where these cells usually operate. Most of the fuel cells in practical applications run at a stoichiometry of an/ca:1.5/2.0, where the 2-D model may not be suitable. While the 1+2D model has few limitations in accounting for in-plane flow dynamics, it still outperforms the 2-D models and can provide insights on cell operation in a time-efficient manner.

5.2.3. Effect of Operating conditions

Using the 1+2D model, the effect of different operating environments on integral cell performance can be studied. The studies in the previous sections have already shown that the flow rates for integral cell must be optimized for reactant concentration and cell hydration. In this section, we examine the impact of other properties on cell performance and recovery. Hydration is quite important for integral cells, especially at lower inlet RH. To understand the impact of cell temperature on cell performance and hydration, 1+2D simulations were carried out at 60°C, 40% RH and varying flowrates as shown in Fig. 12 along with comparison to differential 2-D simulation. Compared to 80°C 40% RH (Fig. 8(a)), the integral simulations at 60°C, 40% RH exhibit significant deviation from the differential data. The difference can be primarily attributed to the ohmic loss overprediction by differential cell. Fig. 13(a-d) shows the cell performance and operating conditions along the channel. Comparing to Fig. 9 (80C, 40%RH), it is seen that the cell saturates faster at 60°C due to primarily the lower saturation vapor pressure at 60°C. The quicker saturation results in better overall RH along the cell, which results in much higher performance than the 2-D differential model that assumes 40% RH throughout. While in differential conditions, the lower temperature result in lower performance, in integral cell, the lower temperature may improve performance under dry conditions.

Another operating strategy is to employ asymmetric RH conditions. Fig. 14 shows the cell performance at 80°C and 30% and 90% RH at cathode and

anode, respectively. The integral model demonstrates better ohmic performance than the differential model at all flow rates, which is due to hydration of cathode down the channel. At lower flow rates, the performance is limited by reactant depletion, while at higher flow rates, the model shows overall better performance than the differential model. Fig. 15 (a-d) shows the conditions down the channel at 0.35 V and different flow rates. The anode RH decreases near the inlet while the cathode get hydrated, which is likely due to water transport from anode to cathode. Once cathode and anode RH are closer, both continue increasing until saturation. Cell performance exhibits a minor dip at the inlet due to anode RH decrease, then recovers and increases due to the cathode RH increase, and finally starts decreasing after both channels are saturated as reactant depletion starts affecting the cell.

To understand the cathode hydration better, the net water flux through the membrane was analyzed. The normalized water flux, β, is defined as the ratio of net flux of water towards cathode to net flux of protons through membrane [22],

$$\beta = \frac{N_{H_2O}}{N_{H^+}} \quad (66)$$

When only the water produced in the ORR is transported across the membrane, the value of β should range between 0 to 0.5. Fig. 16 shows the normalized water flux along the channel at 0.35 V. Near the inlet of the channel, β is higher than 0.5, suggesting that water apart from the ORR is

being transported to the cathode. The region in Fig. 15(b) which corresponds to β>0.5 in Fig. 16 shows anode RH decrease, suggesting that the additional water is being adsorbed and transported from anode side. Once the anode and cathode RH stabilize, only the water generated in ORR is transported across the membrane, thereby bringing the value of β under 0.5. This study suggests that the properties of membrane can also be changed to mitigate dry conditions at cathode. These studies can also be crucial to improve water management in alkaline exchange membrane fuel cells (AEMFCs), where cathode dry out is quite common due to water consumption in cathode.

6. Summary

A pseudo 3D (1+2D) simulation model was developed for predicting integral cell performance from differential data, while still accounting for key effects and phenomena. The model uses a 2-D model combined with an along-the-channel stepping algorithm to account for channel changes in reactant concentration, pressure, temperature, and relative humidity (RH). Crucial cell parameters such as ECSA, water uptake, ionomer conductivity, and agglomerate properties are estimated by fitting the 2-D MEA model to differential experimental data. The same parameters are then used with the 1+2D model to estimate integral cell performance.

Comparison of the 1+2D model predictions against experimental integral data shows that the model can capture the cell behavior at low flow rates and limiting conditions accurately; however, at high flow rates, discrepancies

are observed. In-plane flow profiles are likely the cause of inaccuracy at higher flow rates, which requires more complex models of in-channel transport. In addition, differences in channel architecture between the integral and differential cell setups may also result the discrepancies. At higher RHs, the lack of sufficient channel model that accounts for flooding in the channels, surface blockage and droplet removal may also be needed to close the gap between experiments and simulation. For high surface carbon (HSC) based catalyst layer, accurate knowledge of ECSA change with RH was found to be crucial for estimating kinetic regions of the cell polarization curve.

A study on effect of reactant flow rates demonstrates that optimum flow rates depend on inlet conditions. Flow rates need to be optimized to ensure sufficient RH increase along the channel while keeping the reactant depletion to a minimum. For wet inlet conditions, medium to high flow rates (Stoichiometry>1.5) were found to be optimal, which result in low reactant depletion. On the other hand, intermediate flow rates (1.5< Stoichiometry < 4) were found to be optimum for dry inlet conditions, which result in desired increase in RH along the channel while keeping reactant depletion to non-detrimental values. Comparing the 1+2D modeling results with 2-D differential simulations shows that the differential model is inaccurate at dry inlet conditions and/or at low flow rates. For saturated or near saturated (high RH) inlet conditions, RH changes along the channel are minimal. Under

these conditions, reactant depletion can be estimated using a log-mean mole fraction, and the differential model is able to predict cell performance. The differential model is also limited in modeling integral cells at lower temperature or with asymmetric RH conditions. While the 1+2D model can account for quicker saturation at lower temperature, or for hydration down the channel, the 2-D model cannot.

Overall, our results demonstrate the importance of understanding water management and reactant issues arising due to along the channel changes and show that the 1+2D model is an essential tool to understand integral cell performance. In addition, this study shows that differential data can be used to predict integral cell performance via the 1+2-D model under most practical PEFC operating circumstances. To close the gap between the model and simulation, current experimental studies including segmented cells are being undergone as well as model improvements including ways to account for in-plane transport, effect of channel geometries, and more accurate GDL/ Channel interface models at high RH.

Acknowledgements

This work was funded under the Fuel Cell Performance and Durability Consortium (FC-PAD), by the Fuel Cell Technologies Office (FCTO), Office of Energy Efficiency and Renewable Energy (EERE), of the U.S. Department of Energy under contract number DE-AC02-05CH11231. The authors would like

to thank Prof. Iryna Zenyuk and Dr. Huai Shen Shiau for providing the initial COMSOL model and subsequent discussions. The authors would also like to acknowledge Derek Michael, David Langlois, and Roger Lujan from LANL for their support with the experimental work.

Nomenclature

Abbreviations

BPP	Bi-polar plate
CCM	Catalyst coated membrane
CL	Catalyst layer
GDL	Gas diffusion layer
HOR	Hydrogen reduction reaction
MEA	Membrane electrode assembly
MPL	Micro-porous layer
ORR	Oxygen reduction reaction
PEM	Proton exchange membrane

Roman

a_i	Activity of species/phase i
$A_{v,i}$	Catalyst specific area for electrode i (1/m)
$C_{p,i}$	Mass specific heat capacity of species i (¿
$\acute{C}_{p,i}$	Molar specific heat capacity of species i ($J/mol \cdot K$)
D_{ij}	Maxwell-Stefan diffusion coefficient for species i and j (m^2/s)
$\widetilde{D}_{ij}$	Inverted mass fraction dependent diffusion coefficient for species i and j (m^2/s ¿
E_r	Agglomerate effectiveness factor
EW	Equivalent weight (kg/mol)

F	Faradays constant (C/mol)
h_T	Thiele modulus
H_i	Mass enthalpy of species *i* (J/kg)
$\acute{H}_i$	Molar enthalpy of species *i* (J/mol)
$H_{O_2,m}$	Henry's constant for oxygen dissolution in ionomer ($Pa \cdot m^3/mol$)
i_0	Exchange current density (A/m^2)
$j_{rxn,i}$	Rate of current production in phase *i* (A/m^3)
k_0	Absolute permeability (m^2)
$k_{r,i}$	Relative permeability for phase *i*
$k_{T,i}$	Thermal conductivity of phase *i* ($W/m \cdot K$)
k_i	Transport coefficient related to *i*
M_i	Molecular weight of species *i* (kg/mol)
p_i	Pressure of species/phase *i* (Pa)
r_{agg}	Agglomerate radius (m)
R	Universal gas constant ($J/mol \cdot K$)
RH	Relative humidity
R_i	Rate of generation of species *i*
S_L	Liquid saturation
S_m	Fraction of ionomer equilibrated with liquid
T, T_i	Temperature/ temperature of species *i*(K)
u_i	Velocity of species/phase *i* (m/s)
$\acute{V}_{agg}$	Ratio of agglomerate core volume to total agglomerate volume
$\acute{V}_i$	Molar volume of *i* (m^3/mol)
x_i	Mole fraction of species *i*

Greek

$\alpha_{a,i}$	Anodic transfer coefficient for reaction *i*
$\alpha_{c,i}$	Cathodic transfer coefficient for reaction *i*
$\alpha_{m,i}$	Water diffusion parameter for membrane equilibrated with phase *i* ($S \cdot mol^2/kg \cdot m^3$)
δ_{agg}	Ionomer film thickness on agglomerate core (m)
ϵ_i	Volume fraction of phase *i*
η_i	Overpotential for phase /reaction *i* (V)
γ	Surface tension of water (N/m)
κ_i	Protonic conductivity of phase *i* (S/m)
λ	Membrane water content
μ_i	Viscosity of species/phase *i* ($Pa \cdot s$)
$\acute{\mu}_i$	Chemical potential of species/phase *i* (J/mol)
ω_i	Mass fraction of species *i*

ϕ_i	Electric potential of phase *i* (V)
Π_i	Peltier coefficient for electrode *i* (V)
ρ_i	Density of species/phase *i* (kg/m^3)
σ_i	Electric conductivity of phase *i* (S/m)
τ_i	Tortuosity of phase *i*
$\xi_{m,i}$	Electro-osmotic drag coefficient for membrane equilibrated with phase *i*

Subscripts and superscripts

c	Capillary
eff	Volume averaged effective property
ev	Evaporation
G	Gas phase
gen	Generation
i , j	Phase/species *i, j*
L	Liquid phase
m	Membrane/electrolyte phase
res	Residual
rxn	Reaction
s	Solid phase
sat	Saturation
t	Triple point property
v	Void phase
V	Vapor phase
w	Water (general)

Supplementary material

Supplementary material for this article contains additional non-critical formulation and simulation results and can be retrieved from <DOI LINK: To be added at publication time>.

References

[1] D. Papageorgopoulos, U.S. Department of Energy Hydrogen and Fuel Cells Overview, H2FC-FAIRHannover, Germany, 2013.
[2] D. Papageorgopoulos, Status of DOE EERE's Fuel Cell Research and Development Efforts, Fuel Cell Seminar & ExpositionSan Antonio, TX, 2010.
[3] Handbook of Fuel Cells: Fundamentals Technology and Applications, John Wiley & Sons, Hoboken NJ, 2009.
[4] P. Oberholzer, P. Boillat, Local Characterization of PEFCs by Differential Cells: Systematic Variations of Current and Asymmetric Relative Humidity, J. Electrochem. Soc., 161 (2014) F139-F152.
[5] R.P. Iczkowski, M.B. Cutlip, Voltage Losses in Fuel Cell Cathodes, J. Electrochem. Soc., 127 (1980) 1433-1440.
[6] D.M. Bernardi, M.W. Verbrugge, Mathematical model of a gas diffusion electrode bonded to a polymer electrolyte, AlChE J., 37 (1991) 1151-1163.
[7] D.M. Bernardi, M.W. Verbrugge, Mathematical model of the solid-polymer-electrolyte fuel cell, J. Electrochem. Soc., 139 (1992) 2477-2491.
[8] T.E. Springer, T.A. Zawodzinski, S. Gottesfeld, Polymer electrolyte fuel cell model, J. Electrochem. Soc., 138 (1991) 2334-2342.
[9] M. Eikerling, A.A. Kornyshev, Modelling the performance of the cathode catalyst layer of polymer electrolyte fuel cells, J. Electroanal. Chem., 453 (1998) 89-106.
[10] F. Jaouen, G. Lindbergh, G. Sundholm, Investigation of Mass-Transport Limitations in the Solid Polymer Fuel Cell Cathode I. Mathematical Model, J. Electrochem. Soc., 149 (2002) A437-A447.
[11] M.L. Perry, J. Newman, E.J. Cairns, Mass Transport in Gas-Diffusion Electrodes: A Diagnostic Tool for Fuel-Cell Cathodes, J. Electrochem. Soc., 145 (1998) 5-15.
[12] S.H. Chan, W.A. Tun, Catalyst layer models for proton exchange membrane fuel cells, Chemical Engineering & Technology, 24 (2001) 51-57.
[13] L. You, H. Liu, A parametric study of the cathode catalyst layer of PEM fuel cells using a pseudo-homogeneous model, Int. J. Hydrogen Energy, 26 (2001) 991-999.
[14] T.F. Fuller, J. Newman, Water and Thermal Management in Solid-Polymer-Electrolyte Fuel Cells, J. Electrochem. Soc., 140 (1993) 1218-1225.
[15] C.Y. Wang, W.B. Gu, B.Y. Liaw, Micro-Macroscopic Coupled Modeling of Batteries and Fuel Cells I. Model Development, J. Electrochem. Soc., 145 (1998) 3407-3417.
[16] J.J. Baschuk, X. Li, Modelling of polymer electrolyte membrane fuel cells with variable degrees of water flooding, J. Power Sources, 86 (2000) 181-196.
[17] A.Z. Weber, J. Newman, Transport in polymer-electrolyte membranes. I. Physical model, J. Electrochem. Soc., 150 (2003) A1008-A1015.
[18] A.Z. Weber, J. Newman, Transport in Polymer-Electrolyte Membranes: II. Mathematical Model, J. Electrochem. Soc., 151 (2004) A311-A325.

[19] A.Z. Weber, J. Newman, Transport in Polymer-Electrolyte Membranes III. Model Validation in a Simple Fuel-Cell Model, J. Electrochem. Soc., 151 (2004) A326-A339.
[20] A.Z. Weber, R.M. Darling, J. Newman, Modeling Two-Phase behavior in PEFCs, J. Electrochem. Soc., 151 (2004) A1715-A1727.
[21] A.Z. Weber, J. Newman, Effects of microporous layers in polymer electrolyte fuel cells, J. Electrochem. Soc., 152 (2005) A677-A688.
[22] A.Z. Weber, J. Newman, Coupled thermal and water management in polymer electrolyte fuel cells, J. Electrochem. Soc., 153 (2006) A2205-A2214.
[23] P. Rama, Y. Liu, R. Chen, H. Ostadi, K. Jiang, Y. Gao, X. Zhang, R. Fisher, M. Jeschke, Multiscale modeling of single-phase multicomponent transport in the cathode gas diffusion layer of a polymer electrolyte fuel cell, Energy Fuels, 24 (2010) 3130-3143.
[24] D. Natarajan, T.V. Nguyen, A Two-Dimensional, Two-Phase, Multicomponent, Transient Model for the Cathode of a Proton Exchange Membrane Fuel Cell Using Conventional Gas Distributors, J. Electrochem. Soc., 148 (2001) A1324-A1335.
[25] W. Sun, B.A. Peppley, K. Karan, An improved two-dimensional agglomerate cathode model to study the influence of catalyst layer structural parameters, Electrochim. Acta, 50 (2005) 3359-3374.
[26] G. Lin, T.V. Nguyen, A Two-Dimensional Two-Phase Model of a PEM Fuel Cell, J. Electrochem. Soc., 153 (2006) A372-A382.
[27] R.J. Balliet, J. Newman, Cold Start of a Polymer-Electrolyte Fuel Cell I. Development of a Two-Dimensional Model, J. Electrochem. Soc., 158 (2011) B927-B938.
[28] M. Bhaiya, A. Putz, M. Secanell, Analysis of non-isothermal effects on polymer electrolyte fuel cell electrode assemblies, Electrochim. Acta, 147 (2014) 294-309.
[29] M. Secanell, A. Putz, P. Wardlaw, V. Zingan, M. Bhaiya, M. Moore, J. Zhou, C. Balen, K. Domican, OpenFCST: An open-source mathematical modelling software for polymer electrolyte fuel cells, ECS Trans., 64 (2014) 655-680.
[30] L. Xing, X. Liu, T. Alaje, R. Kumar, M. Mamlouk, K. Scott, A two-phase flow and non-isothermal agglomerate model for a proton exchange membrane (PEM) fuel cell, Energy, 73 (2014) 618-634.
[31] I.V. Zenyuk, P.K. Das, A.Z. Weber, Understanding Impacts of Catalyst-Layer Thickness on Fuel-Cell Performance via Mathematical Modeling, J. Electrochem. Soc., 163 (2016) F691-F703.
[32] I.V. Zenyuk, E. Medici, J. Allen, A.Z. Weber, Coupling continuum and pore-network models for polymer-electrolyte fuel cells, Int. J. Hydrogen Energy, 40 (2015) 16831-16845.
[33] J. Zhou, A. Putz, M. Secanell, A Mixed Wettability Pore Size Distribution Based Mathematical Model for Analyzing Two-Phase Flow in Porous Electrodes I. Mathematical Model, J. Electrochem. Soc., 164 (2017) F530-F539.

[34] J. Zhou, S. Shukla, A. Putz, M. Secanell, Analysis of the role of the microporous layer in improving polymer electrolyte fuel cell performance, Electrochim. Acta, 268 (2018) 366-382.
[35] J. Zhou, D. Stanier, A. Putz, M. Secanell, A Mixed Wettability Pore Size Distribution Based Mathematical Model for Analyzing Two-Phase Flow in Porous Electrodes II. Model Validation and Analysis of Micro-Structural Parameters, J. Electrochem. Soc., 164 (2017) F540-F556.
[36] J.S. Yi, T.V. Nguyen, An Along-the-Channel Model for Proton Exchange Membrane Fuel Cells, J. Electrochem. Soc., 145 (1998) 1149-1159.
[37] J.S. Yi, T.V. Nguyen, Multicomponent Transport in Porous Electrodes of Proton Exchange Membrane Fuel Cells Using the Interdigitated Gas Distributors, J. Electrochem. Soc., 146 (1999) 38-45.
[38] J.S. Yi, J.D. Yang, C. King, Water management along the flow channels of PEM fuel cells, AlChE J., 50 (2004) 2594-2603.
[39] S. Um, C.Y. Wang, K.S. Chen, Computational Fluid Dynamics Modeling of Proton Exchange Membrane Fuel Cells, J. Electrochem. Soc., 147 (2000) 4485-4493.
[40] Z.H. Wang, C.Y. Wang, K.S. Chen, Two-phase flow and transport in the air cathode of proton exchange membrane fuel cells, J. Power Sources, 94 (2001) 40-50.
[41] N.P. Siegel, M.W. Ellis, D.J. Nelson, M.R. Von Spakovsky, Single domain PEMFC model based on agglomerate catalyst geometry, J. Power Sources, 115 (2003) 81-89.
[42] A.Z. Weber, J. Newman, Effects of Membrane- and Catalyst-Layer-Thickness Nonuniformities in Polymer-Electrolyte Fuel Cells, J. Electrochem. Soc., 154 (2007) B405-B412.
[43] G.A. Futter, P. Gazdzicki, K.A. Friedrich, A. Latz, T. Jahnke, Physical modeling of polymer-electrolyte membrane fuel cells: Understanding water management and impedance spectra, J. Power Sources, 391 (2018) 148-161.
[44] S. Dutta, S. Shimpalee, J.W.V. Zee, Three-dimensional numerical simulation of straight channel PEM fuel cells, J. Appl. Electrochem., 30 (2000) 135-146.
[45] S. Um, C.Y. Wang, Three-dimensional analysis of transport and electrochemical reactions in polymer electrolyte fuel cells, J. Power Sources, 125 (2004) 40-51.
[46] W. Ying, T.-H. Yang, W.-Y. Lee, J. Ke, C.-S. Kim, Three-dimensional analysis for effect of channel configuration on the performance of a small air-breathing proton exchange membrane fuel cell (PEMFC), J. Power Sources, 145 (2005) 572-581.
[47] H.-C. Chiu, J.-H. Jang, W.-M. Yan, H.-Y. Li, C.-C. Liao, A three-dimensional modeling of transport phenomena of proton exchange membrane fuel cells with various flow fields, Applied Energy, 96 (2012) 359-370.
[48] N. Ahmadi, S. Rezazadeh, I. Mirzaee, N. Pourmahmoud, Three-dimensional computational fluid dynamic analysis of the conventional PEM fuel cell and investigation of prominent gas diffusion layers effect, Journal of Mechanical Science and Technology, 26 (2012) 2247-2257.

[49] U. Pasaogullari, C.-Y. Wang, Two-phase transport and the role of micro-porous layer in polymer electrolyte fuel cells, Electrochim. Acta, 49 (2004) 4359-4369.
[50] U. Pasaogullari, C.-Y. Wang, Two-Phase Modeling and Flooding Prediction of Polymer Electrolyte Fuel Cells, J. Electrochem. Soc., 152 (2005) A380-A390.
[51] M. He, Z. Huang, P. Sun, C. Wang, Modeling and Numerical Studies for a 3D Two-Phase Mixed-Domain Model of PEM Fuel Cell, J. Electrochem. Soc., 160 (2013) F324-F336.
[52] Z. Zhang, W. Liu, Y. Wang, Three dimensional two-phase and non-isothermal numerical simulation of multi-channels PEMFC, Int. J. Hydrogen Energy, (2018).
[53] F.C. Cetinbas, S.G. Advani, A.K. Prasad, Three dimensional proton exchange membrane fuel cell cathode model using a modified agglomerate approach based on discrete catalyst particles, J. Power Sources, 250 (2014) 110-119.
[54] V. Gurau, H. Liu, S. Kakaç, Two-dimensional model for proton exchange membrane fuel cells, AlChE J., 44 (1998) 2410-2422.
[55] W. He, J.S. Yi, T. Van Nguyen, Two-phase flow model of the cathode of PEM fuel cells using interdigitated flow fields, AlChE J., 46 (2000) 2053-2064.
[56] W. Huang, B. Zhou, A. Sobiesiak, Along-channel mathematical modelling for proton exchange membrane fuel cells, International Journal of Energy Research, 29 (2005) 1051-1071.
[57] A.Z. Weber, Gas-Crossover and Membrane-Pinhole Effects in Polymer-Electrolyte Fuel Cells, J. Electrochem. Soc., 155 (2008) B521-B531.
[58] Y.-S. Chen, H. Peng, A segmented model for studying water transport in a PEMFC, J. Power Sources, 185 (2008) 1179-1192.
[59] A. Goshtasbi, B.L. Pence, T. Ersal, Computationally Efficient Pseudo-2D Non-Isothermal Modeling of Polymer Electrolyte Membrane Fuel Cells with Two-Phase Phenomena, J. Electrochem. Soc., 163 (2016) F1412-F1432.
[60] D. Natarajan, T. Van Nguyen, Three-dimensional effects of liquid water flooding in the cathode of a PEM fuel cell, J. Power Sources, 115 (2003) 66-80.
[61] J.O. Schumacher, J. Eller, G. Sartoris, T. Colinart, B.C. Seyfang, 2+1D modelling of a polymer electrolyte fuel cell with glassy-carbon microstructures, Mathematical and Computer Modelling of Dynamical Systems, 18 (2012) 355-377.
[62] L.M. Pant, Z. Yang, M.L. Perry, A.Z. Weber, Development of a Simple and Rapid Diagnostic Method for Polymer-Electrolyte Fuel Cells, J. Electrochem. Soc., 165 (2018) F3007-F3014.
[63] R. Taylor, R. Krishna, Multicomponent Mass Transfer, Wiley1993.
[64] W. Kauzman, Kinetic Theory of Gases, Dover Publications Inc., New York, 2012.
[65] A.Z. Weber, Modeling water management in polymer -electrolyte fuel cells, University of California, Berkeley, 2004.

[66] R. O'Hayre, S.W. Cha, W. Colella, F.B. Prinz, Fuel Cell Fundamentals, 2 ed., Wiley, New York, USA, 2008.
[67] M. Moore, P. Wardlaw, P. Dobson, J.J. Boisvert, A. Putz, R.J. Spiteri, M. Secanell, Understanding the Effect of Kinetic and Mass Transport Processes in Cathode Agglomerates, J. Electrochem. Soc., 161 (2014) E3125-E3137.
[68] F.M. White, Fluid Mechanics, Mcgraw Hill1986.
[69] S.T. Revankar, P. Majumdar, Fuel Cells: Principles, Design, and Analysis, 1 ed., CRC Press, Boca Raton, 2014.
[70] D.P. Wilkinson, O. Vanderleeden, Serpentine Flow field Design, in: W. Vielstich, H.A. Gasteiger, A. Lamm (Eds.) Handbook of Fuel Cells: Fundamentals Technology and Applications, John Wiley & Sons, Hoboken NJ, 2009.
[71] Z. Jingxin, P. Lesley, N. Amit, M. Rohit, Methods and processes to recover voltage loss of pem fuel cell stack, in: U.P.a.T. Office (Ed.), GM Global Technology Operations LLC, USA, 2011.
[72] E. Padgett, N. Andrejevic, Z. Liu, A. Kongkanand, W. Gu, K. Moriyama, Y. Jiang, S. Kumaraguru, T.E. Moylan, R. Kukreja, D.A. Muller, Connecting Fuel Cell Catalyst Nanostructure and Accessibility Using Quantitative Cryo-STEM Tomography, J. Electrochem. Soc., 165 (2018) F173-F180.
[73] A. Kusoglu, A.Z. Weber, New Insights into Perfluorinated Sulfonic-Acid Ionomers, Chem. Rev., 117 (2017) 987-1104.
[74] F.C. Cetinbas, R.K. Ahluwalia, N.N. Kariuki, D.J. Myers, Agglomerates in Polymer Electrolyte Fuel Cell Electrodes: Part I. Structural Characterization, J. Electrochem. Soc., 165 (2018) F1051-F1058.
[75] N.B. Carrigy, L.M. Pant, S. Mitra, M. Secanell, Knudsen diffusivity and permeability of pemfc microporous coated gas diffusion layers for different polytetrafluoroethylene loadings, J. Electrochem. Soc., 160 (2013) F81-F89.
[76] L.M. Pant, S.K. Mitra, M. Secanell, Absolute permeability and Knudsen diffusivity measurements in PEMFC gas diffusion layers and micro porous layers, J. Power Sources, 206 (2012) 153-160.
[77] B. Kientiz, H. Yamada, N. Nonoyama, A.Z. Weber, Interfacial Water Transport Effects in Proton-Exchange Membranes, Journal of Fuel Cell Science and Technology, 8 (2010) 011013-011013-011017.
[78] R.J. Balliet, Modeling Cold Start in a Polymer-Electrolyte Fuel Cell, University of California, Berkeley, Berkeley, 2010.
[79] R. Schweiss, C. Meiser, T. Damjanovic, I. Galbati, N. Haak, SIGRACET Gas Diffusion Layers for PEM Fuel Cell, Electrolyzers and Batteries, in: S.G.T.C. Company (Ed.), SGL Group The Carbon Company, 2018.

List of Tables

List of Figures

Table 1. Transport properties and correlation coefficients of different cell components. Thermal conductivity for all layers are effective conductivities, except for membrane, which is bulk property.

Property	**Plate**	**GDLs**	**MPLs**	**CLs**	**Membrane**
Gas diffusion tortuosity exponent $\beta_{\tau,G}$ [31]		3	1.5	1.5	
Gas relative permeability exponent β_G [31]		3	3	3	
Liquid relative permeability exponent β_L		3.5	3	3	
Absolute permeability $k_0(m^2)$ [75, 76]		1×10^{-11}	1×10^{-13}	1×10^{-13}	
Electron transport tortuosity exponent $\beta_{\tau,s}$	0	0.5	0.5	0.5	
Bulk electronic conductivity σ_s ($S\cdot m^{-1}$)	2×10^{4}	1.2×10^{4}	1.2×10^{4}	1.2×10^{4}	
Proton conduction tortuosity factor $\beta_{\tau,m}$				0.5	0
Thermal conductivity ($W\cdot m^{-1}\cdot K^{-1}$)	25	1.4	0.27	0.27	0.2

Table 2. Source terms for different transport equations

Source Term	GDLs and MPLs	cCL	aCL	Membrane	Plate
R_{H_2}	0	0	$\frac{-j_a}{2F}$		
R_{O_2}	0	$\frac{-j_c}{4F}$	0		
R_V	R_{ev}	$R_{ev}+R_{V,m}$	$R_{ev}+R_{V,m,}$		
R_G	R_{ev}	$\frac{-j_c}{4F}+R_{ev}+R_{V,}$	$\frac{-j_a}{2F}+R_{ev}+R_{V,}$		
R_L	$-R_{ev}$	$-R_{ev}+R_{L,m}$	$-R_{ev}+R_{L,m}$		
$j_{rxn,s}$	0	j_c	$-j_a$		0
$j_{rxn,m}$	0	$-j_c$	j_a		0
$R_{w,m}$		$\frac{j_c}{2F}-R_{V,m}-R$	$-R_{V,m}-R_{L,m}$	0	
Q_{gen}	$Q_{ohm,s}+Q_{ev}$	$Q_{ohm,s}+Q_{ohm,}$	$Q_{ohm,s}+Q_{ohm.r}$	$Q_{ohm,m}$	$Q_{ohm,s}$

Table 3. List of physical parameters/properties for estimating source terms for different transport equations

	Name	Value/expression
Evaporation/ condensation	k_{ev}	$10[kg\cdot mol\cdot J^{-1}\cdot m^{-3}\cdot s^{-1}]$
Adsorption/ desorption [73, 77]	$k_{V,m}$	$10\exp\left(4.48a_w\right)[mol^2\cdot J^{-1}\cdot m^{-3}\cdot s^{-1}]$
	$k_{L,m}$	$1[mol^2\cdot J^{-1}\cdot m^{-3}\cdot s^{-1}]$
Anode Kinetics [31]	p_{ref}	$1\times10^5 Pa$
	$i_{0,a}$	$215\left[A\cdot m^{-2}\right]\exp\left[\frac{17000\left[J\cdot mol^{-1}\right]}{R}\left(\frac{1}{T_t}-\frac{1}{T}\right)\right]$
	$\alpha_{a,HOR}$	1
	$\alpha_{c,HOR}$	1
Cathode Kinetics [67, 78]	$H_{O_2,m}$	$3.166\times10^4\left[Pa\cdot m^3\cdot mol^{-1}\right]$
	$D_{O_2,m}$	$1.3926\times10^{-10}\lambda^{0.708}\exp\left(\frac{T-273.15}{106.65}\right)-1.6461\times10^{-1}$
	$c_{O_2}^{ref}$	$0.85[mol\cdot m^{-3}]$
	$i_{0,c}$	$0.125\left[A\cdot m^{-2}\right]\exp\left[\frac{28921\left[J\cdot mol^{-1}\right]}{R}\left(\frac{1}{353.15\left[K\right]}-\frac{1}{T}\right)\right]$
	$\alpha_{c,ORR}$	$0.495+2.3\times10^{-3}[K^{-1}](T-300\left[K\right])$
	E_{OCV}	$1.23-9\times10^{-4}[K^{-1}]\left(T-298\left[K\right]\right)$
Reaction Heat [22]	Π_a	$-0.012\left[V\right]\frac{T}{T_t}$
	Π_c	$-0.22\left[V\right]\frac{T}{T_t}.$

Table 4. List of boundary conditions for different variables

Variable	Boundary condition	Boundary

$\omega_R, R \in [$	$\omega_R = \frac{x_{R,\in ¿ M_R}}{\sum_i x_{j,\in ¿ M_j}, x_{j,\in ¿ = (1 - x_V^{¿}) x_{R,\in ¿^{dry}¿}}}$ ¿	Anode CH|GDL, Cathode CH|GDL
ω_V	$\omega_V = \frac{x_{V,\in ¿ M_V}}{\sum_i x_{j,\in ¿ M_j}, x_{V,\in ¿ = \frac{RH_¿ p_V^{sat}}{p_G}¿}}$ ¿	Anode CH|GDL, Cathode CH|GDL
ω_{N_2}	$\omega_{N_2} = 1 - \omega_R - \omega_V$	Anode CH|GDL, Cathode CH|GDL
p_G	$p_G = p_{G,\in ¿¿}$	Anode CH|GDL, Cathode CH|GDL
p_L	$\hat{n} \cdot N_L = k_L \frac{(p_L - p_{thru})}{1[Pa]} \left[\tanh\left(\frac{p_L - p_{thru}}{1[Pa]} \right) + 1 \right]$	Anode CH|GDL, Cathode CH|GDL
ϕ_s	$\phi_s = 0$ $\phi_s = \phi_{cell}$ (Potentiostatic), or $\hat{n} \cdot i_s = i_{cell}$ (Galvanostatic)	Anode CH|GDL Cathode CH|GDL
ϕ_m	$\hat{n} \cdot i_m = 0$	Anode CL|MPL, Cathode CL|MPL
μ_w	$\hat{n} \cdot N_{w,m} = 0$	Anode CL|MPL, Cathode CL|MPL
T	$\hat{n} \cdot k_T^{eff} \nabla T = h_{cool}(T - T_{cool})$ $\hat{n} \cdot k_T^{eff} \nabla T = h_{chan}(T - T_{chan})$	Anode BPP|cool, Cathode BPP|cool Anode GDL|chan, Cathode GDL|chan

Table 5. Properties and operating conditions used for differential cell analysis

Property	Value

Operating conditions	Anode/cathode channel pressure	150 kPa
	Anode channel x_{H_2}	1.0
	Cathode channel x_{O_2}	0.21
	Coolant/channel temperature	60 or 80°C
	Anode/cathode relative humidity	40%, 60%, 80%, or 100%
Geometric parameters	Anode/cathode GDL thickness [79]	190 μm
	Anode/cathode MPL thickness [79]	45 μm
	Anode CL thickness (SEM measurement)	9.45 μm
	Cathode CL thickness (SEM measurement)	6.67 μm
	Membrane thickness (SEM measurement)	19 μm
	Bi-polar plate thickness	0.5 mm
Electrode physical properties	Anode/cathode GDL porosity	0.7
	Anode/cathode MPL porosity	0.62
	Anode CL porosity	0.6
	Cathode CL porosity	0.5
	Anode CL ionomer volume fraction	0.18
	Cathode CL ionomer volume fraction	0.19
	Anode specific ECSA	5.4×10^6 m^{-1}
Agglomerate properties	Agglomerate radius (r_{agg}) [31]	50 [nm]
	Agglomerate core ionomer fraction ($\epsilon_{m,agg}$) [31]	0.5
Boundary condition constants	Liquid flux constant (k_L)	$10^{-1}[kg \cdot m^{-2} \cdot s^{-1}]$
	Coolant heat transfer coefficient (h_{cool})	$5 \times 10^3[W \cdot m^{-2} \cdot K^{-1}]$
	Channel heat transfer coefficient (h_{chan})	$3 \times 10^2[W \cdot m^{-2} \cdot K^{-1}]$
Fitting parameters	Cathode ECSA	
	Ionomer water uptake (λ_V)	
	Ionomer conductivity in liquid ($\kappa_{m,L}$)	
	Agglomerate film thickness (δ_{agg})	

Table 6. Simulated cathode stoichiometry at 80C, 0.3V and varying operating conditions

Flow rate Anode/cathode ($L \cdot min^{-1}$)	Cathode O_2 stoichiometry at 0.3 V	
	40% RH	80RH
0.2/0.4	1.0	1.0
0.4/0.8	1.01	1.0
1.0/2.0	1.67	1.32
2.0/4.0	3.88	Not simulated
3.0/5.0	5.17	Not simulated

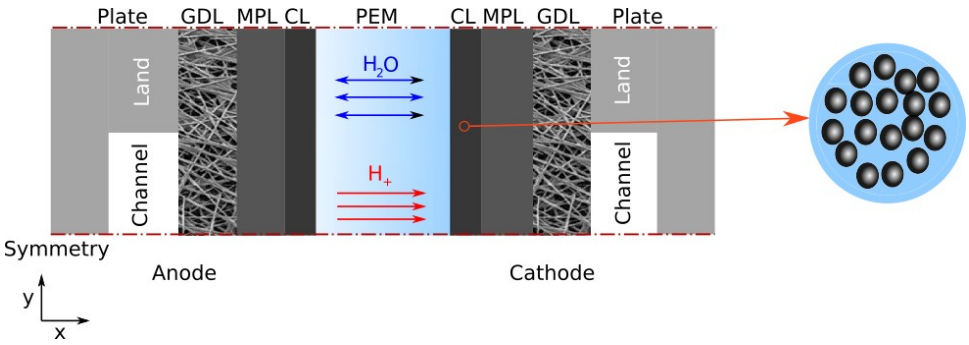

Fig. 1. Modeling domain of 2-D MEA cross-section with an inset view of cathode agglomerates. Image not to scale.

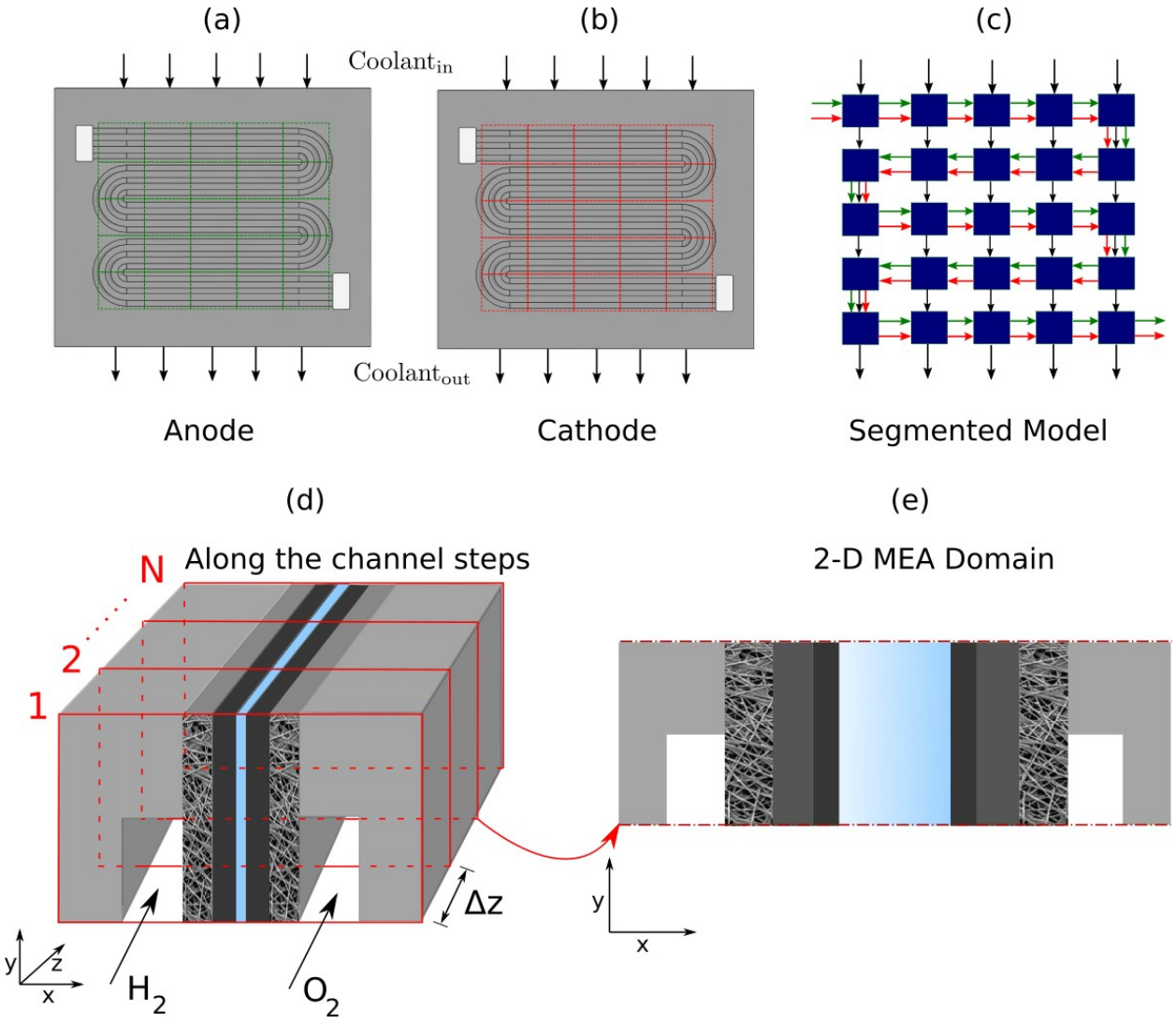

Fig. 2. Illustration of a segmented cell approach. (a-c) show in-plane illustration with a triple serpentine channel co-flow cell with cross-flow coolant. (a) Flow

channel design of anode showing segments in green blocks, (b) flow channel design for cathode showing segments in red blocks, (c) Connected segments modeling approach, (d) Schematics of the along the channel simulation method using (e) the 2-D MEA model.

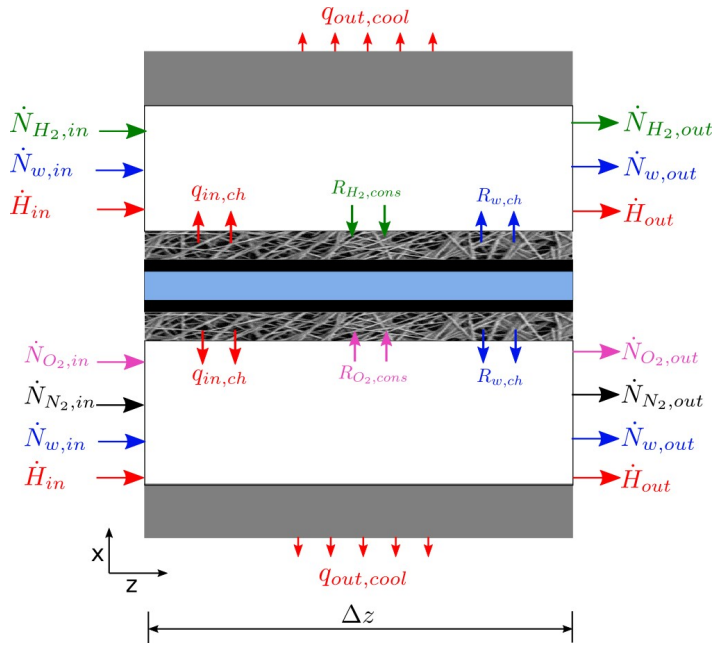

Fig. 3. (Color online) Illustration of species and energy transport in a cell segment along the channel

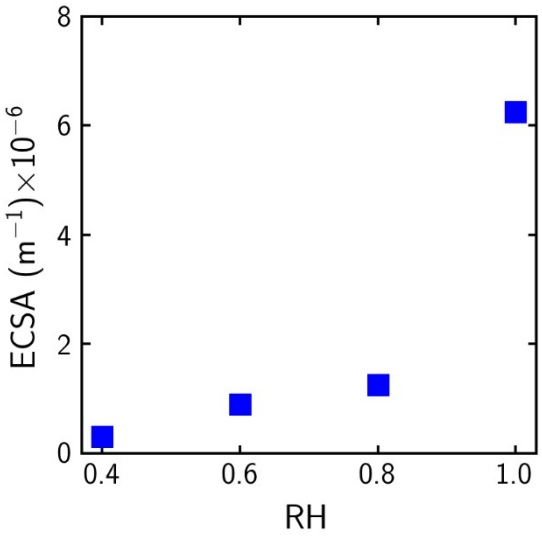

Fig. 4. Fit ECSA value for cathode CL at different RH values

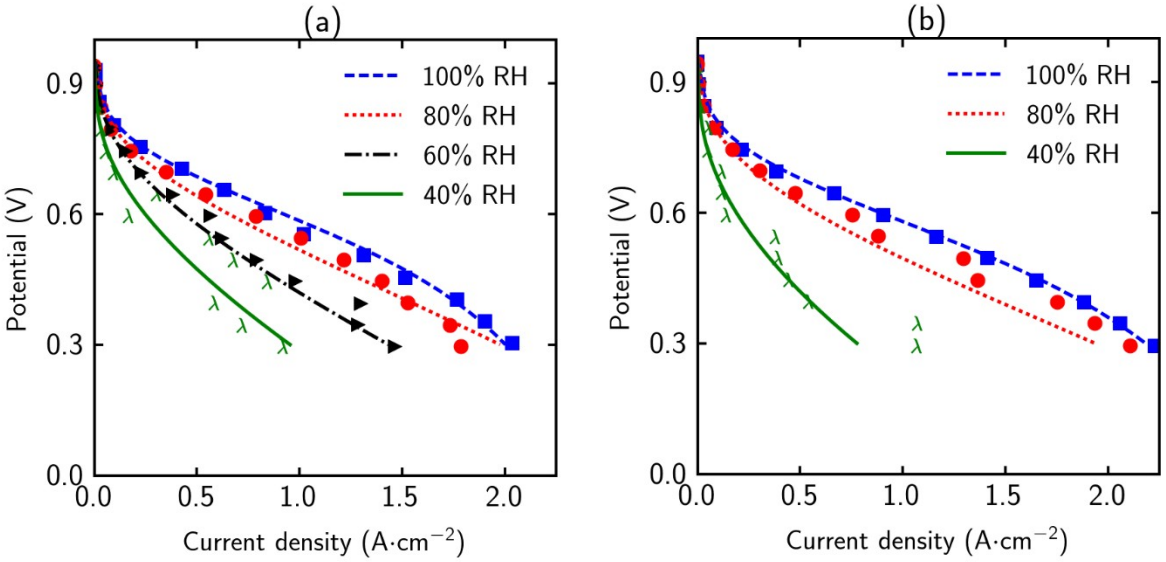

Fig. 5. (Color online) Comparison of the differential experimental polarization curves with the 2-D model predictions at different operating conditions (lines are the simulated results and points are experimental data) (a) 80°C, (b) 60°C

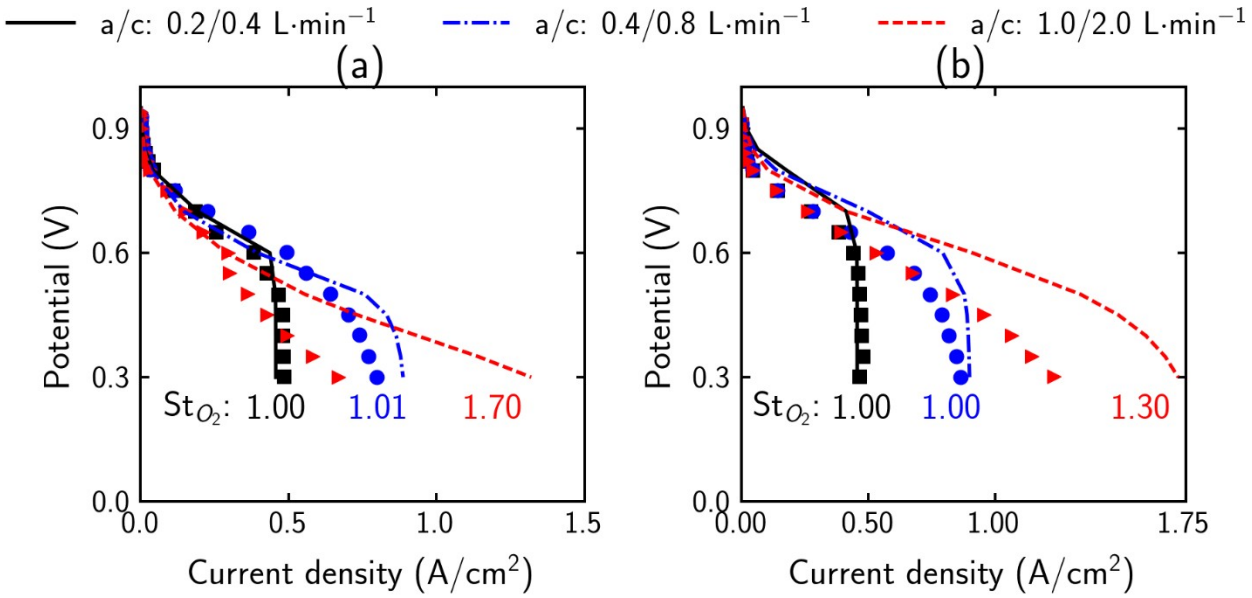

Fig. 6. (Color online) Comparison of experimental integral cell performance with 1+2D model estimations at 80 C and different reactant flow rates. Points are experimental data and lines are simulations. The mentioned stoichiometry is for cathode and calculated at maximum current in the model. (a) 40% RH, (b) 80% RH

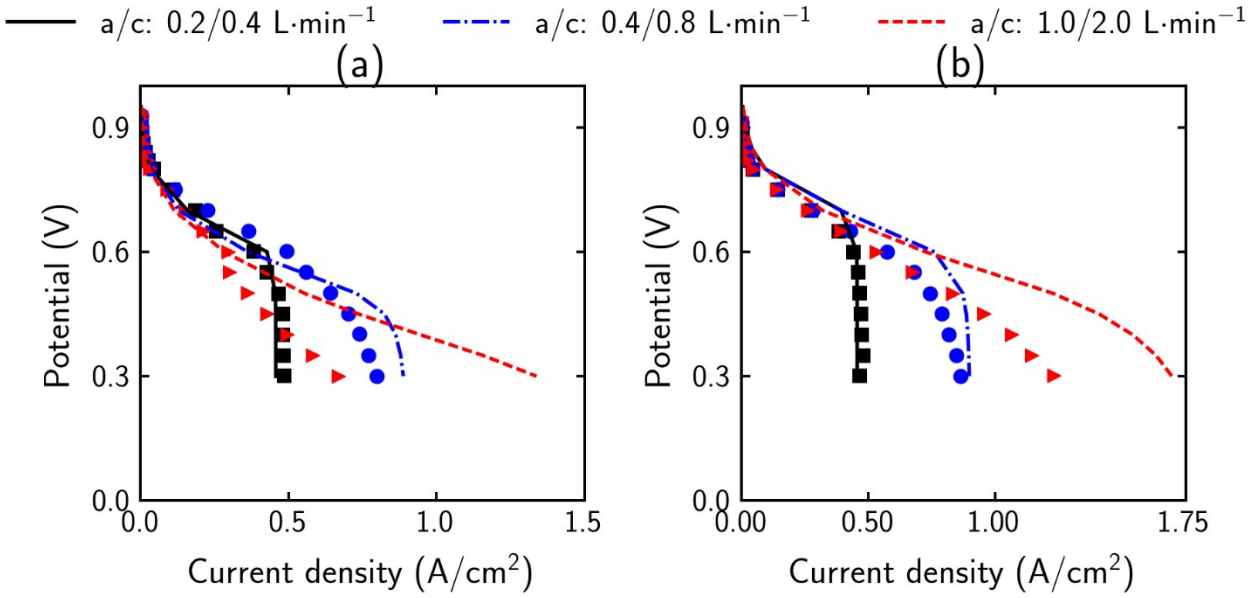

Fig. 7. (Color online) Comparison of experimental integral cell performance with 1+2D model estimations with different ECSA trend at 80 C and different reactant flow rates. Points are experimental data and lines are simulations. (a) 40% RH, (b) 80% RH

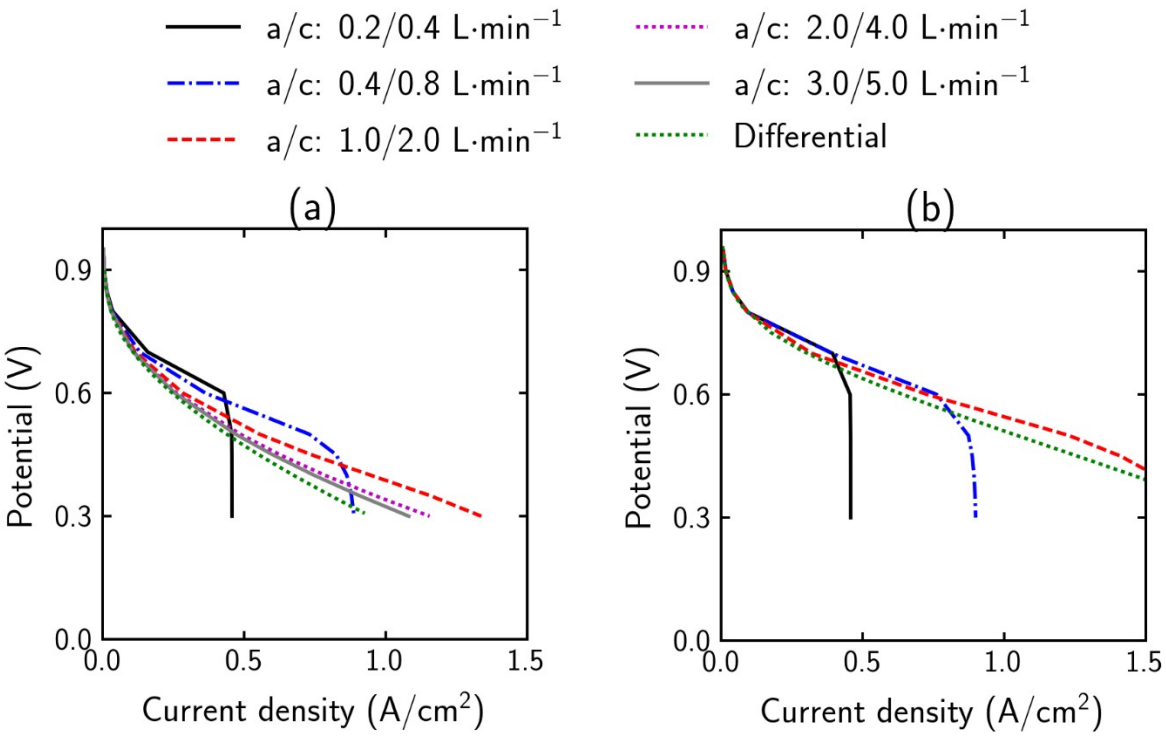

Fig. 8. (Color online) Effect of reactant flow rate on integral cell performance and comparison to differential cell at 80C. (a) 40% RH, (b) 80%RH.

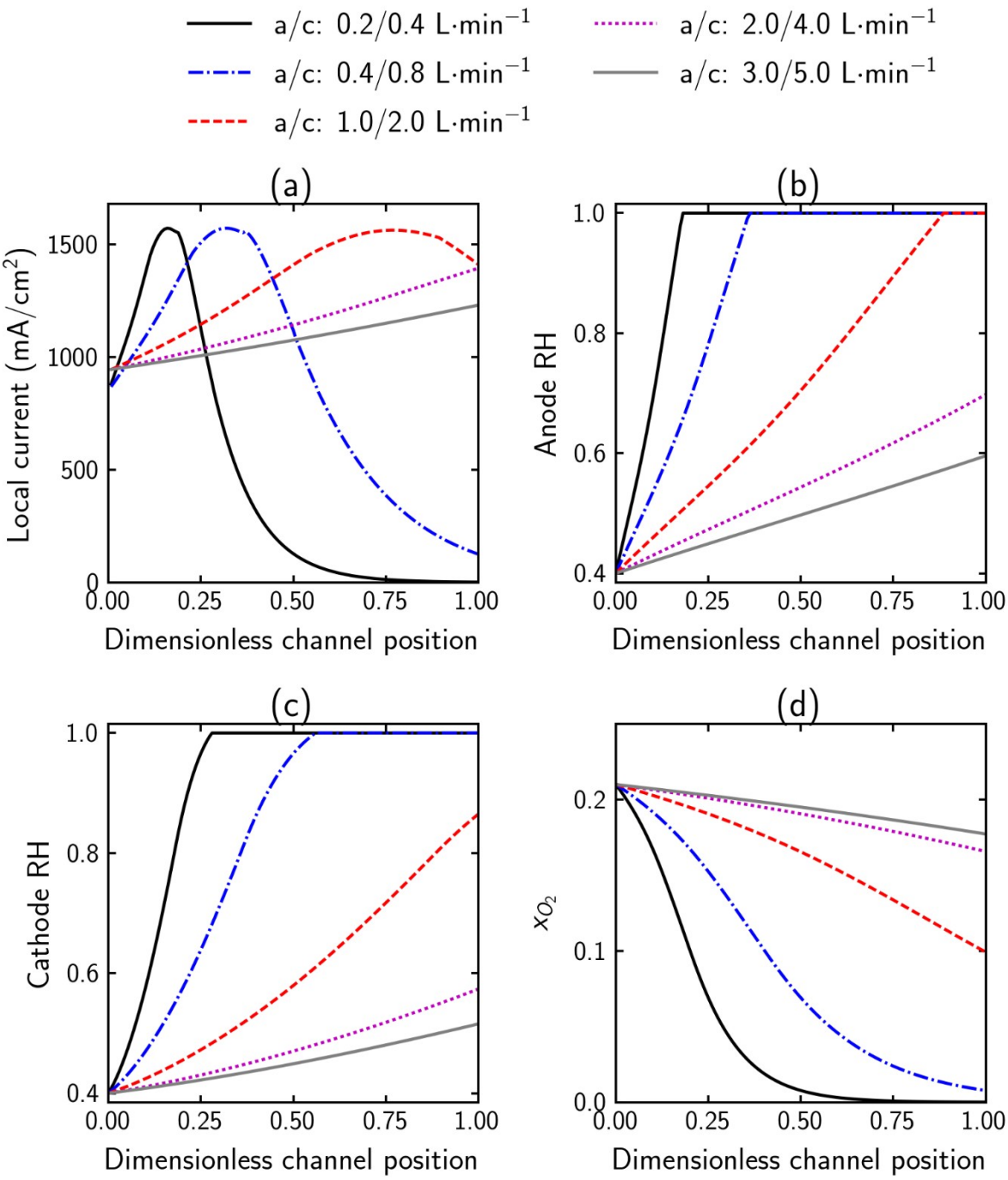

Fig. 9. (Color online) Evolution of operating conditions along the channel for varying flowrates and at 0.3V, 80C and 40% RH at cell inlet. (a) Anode RH, (b) Cathode RH, and (c) Cathode oxygen mole fraction

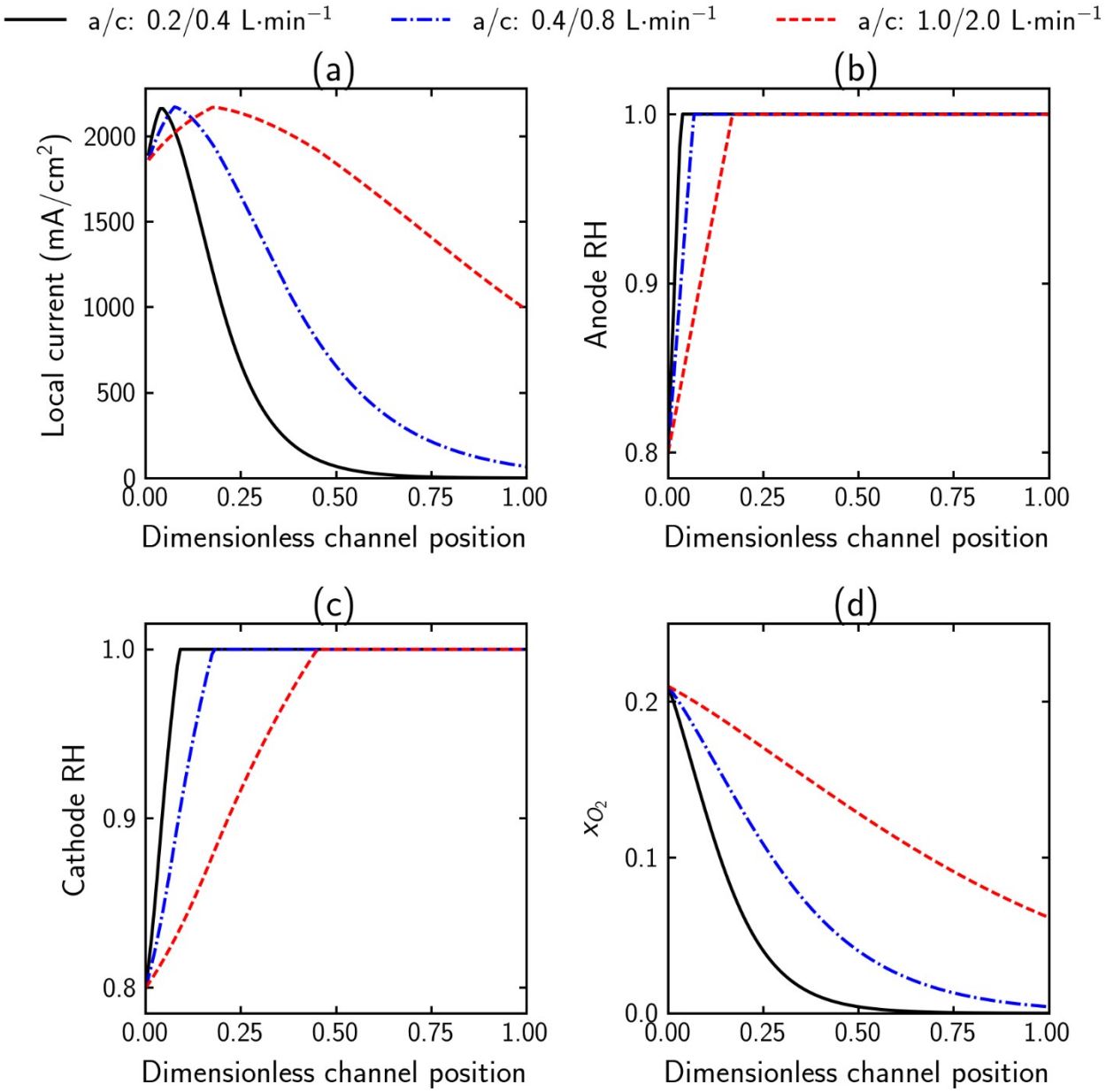

Fig. 10. (Color online) Evolution of operating conditions along the channel for varying flowrates and at 0.3V, 80C and 80% RH at cell inlet. (a) Anode RH, (b) Cathode RH, and (c) Cathode oxygen mole fraction

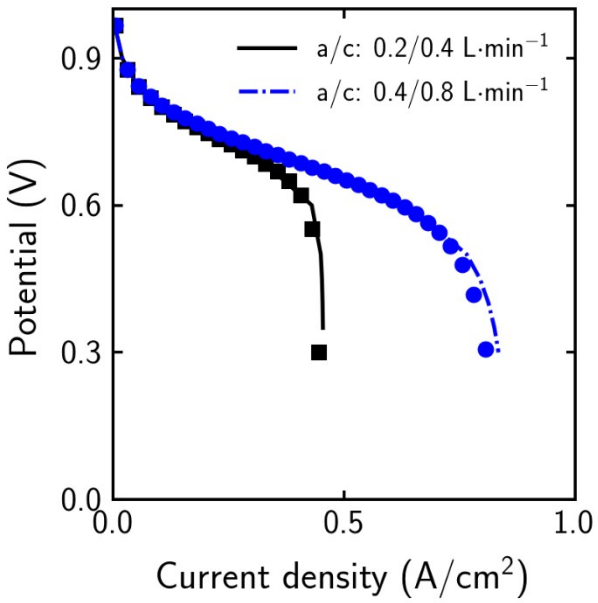

Fig. 11. (Color online) Comparison of integral and differential simulation results at 80C, 100%RH, and different flow rates. Points are integral simulation data and lines are differential simulations

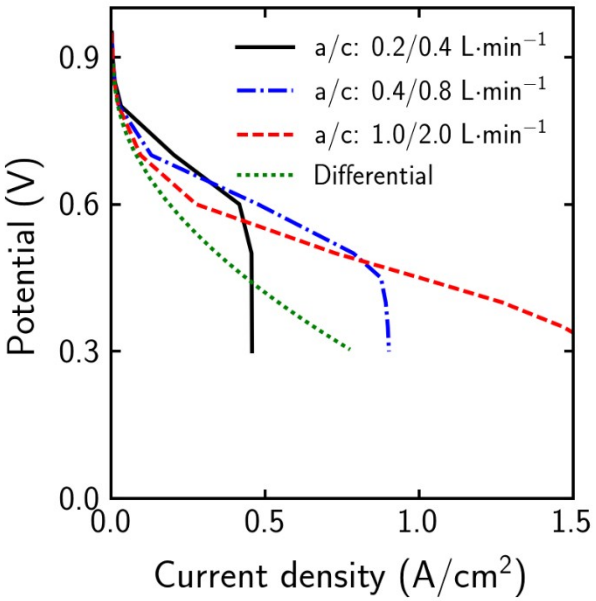

Fig. 12. (Color online) Effect of reactant flow rate on integral cell performance and comparison to differential cell at 60C and 40% inlet RH.

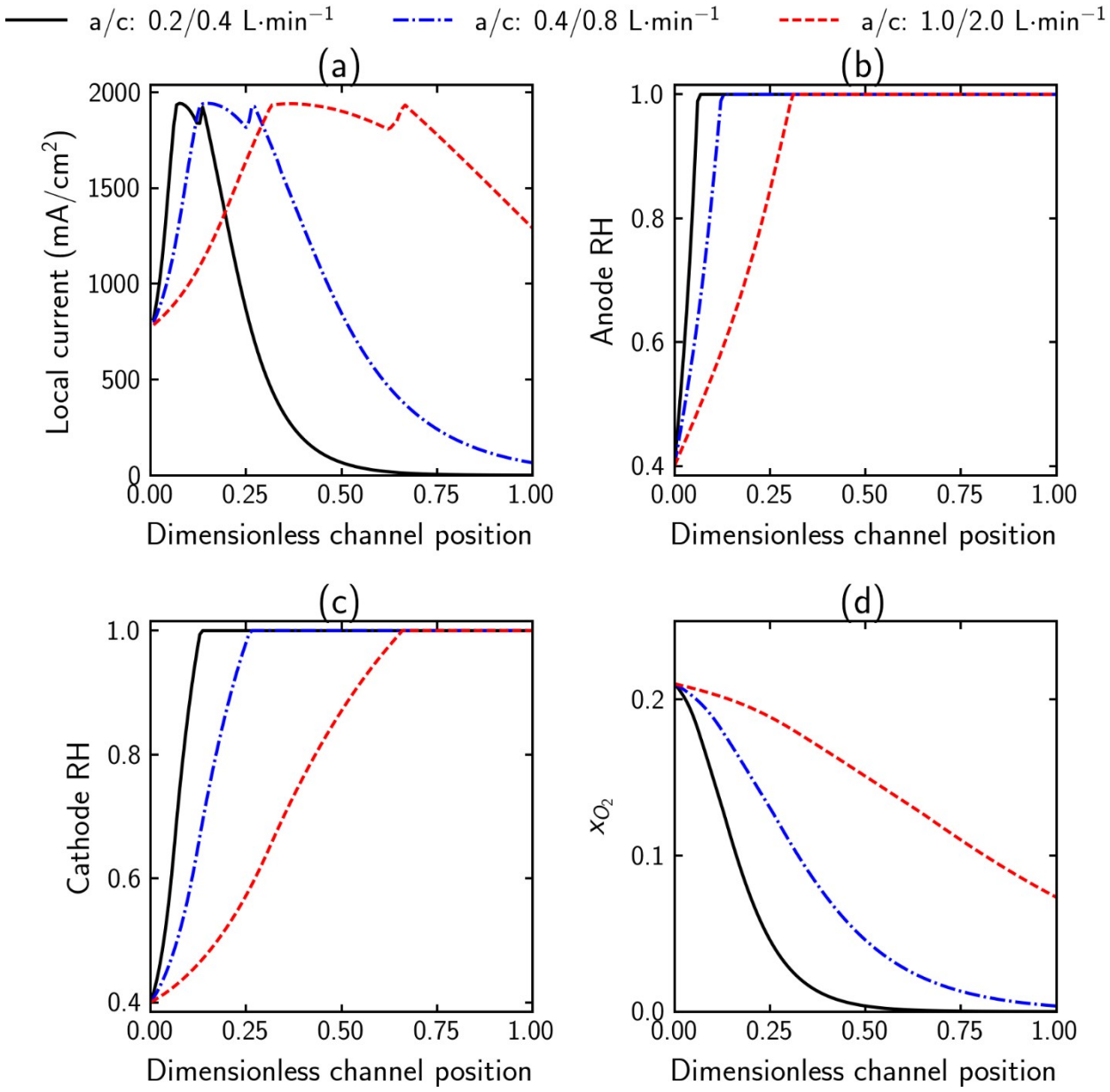

Fig. 13. (Color online) Evolution of operating conditions along the channel for varying flowrates and at 0.3V, 60°C and 40% RH at cell inlet. (a) Local current density, (b) Anode RH, (c) Cathode RH, and (d) Cathode oxygen mole fraction

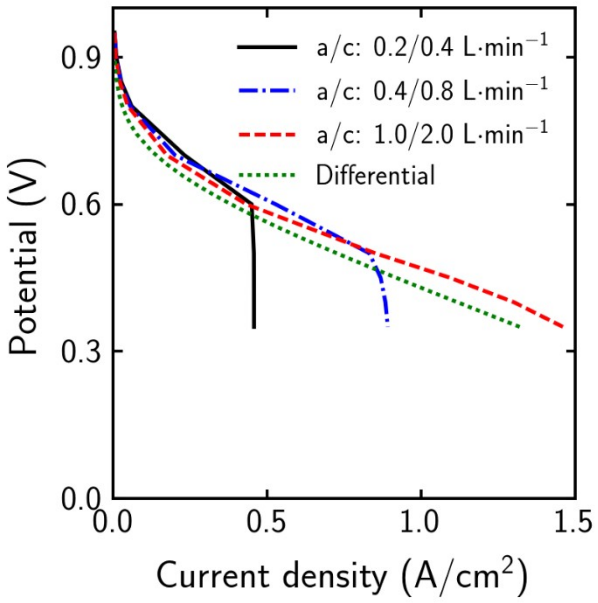

Fig. 14. (Color online) Effect of reactant flow rate on an integral cell performance with asymmetric RH and comparison to differential cell at 80°C and 30% & 90% inlet RH at cathode and anode respectively.

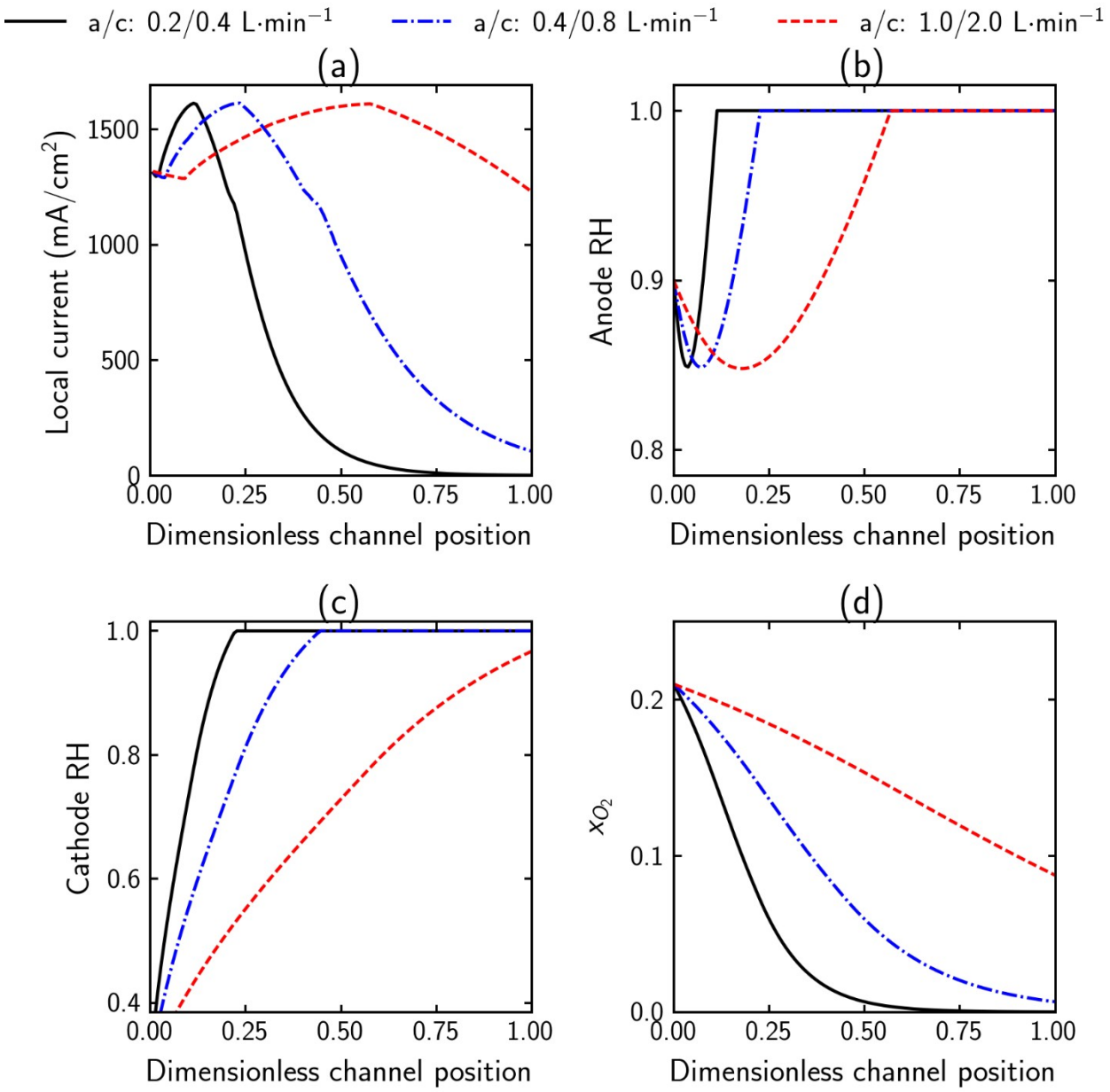

Fig. 15. (Color online) Evolution of operating conditions along the channel for varying flowrates and at 0.35V, 80°C and 30% & 90% RH at cathode and anode inlet

respectively. (a) Current density, (b) Anode RH, (c) Cathode RH, and (d) Cathode oxygen mole fraction

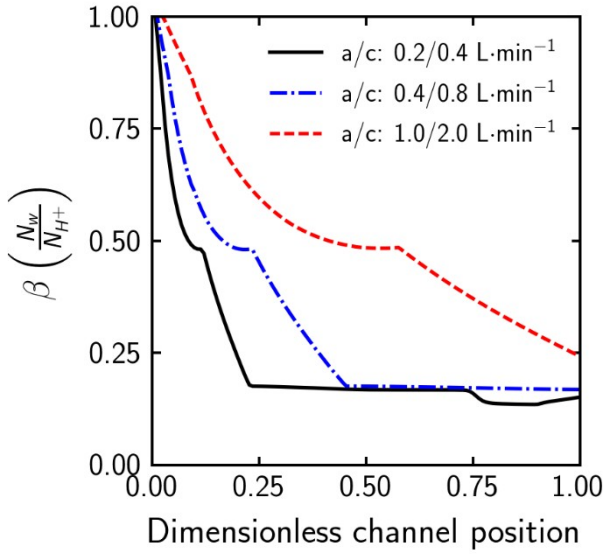

Fig. 16. (Color online) Normalized water flux across the membrane at 0.35V, 80C and 30% & 90% RH at cathode and anode inlet respectively